

Lehrstuhl für Informatik 10 (Systemsimulation)



**Optimization of mirror shapes in optically pumped solar lasers using
ray tracing simulation techniques**

Matthias König

Master's Thesis

Optimization of mirror shapes in optically pumped solar lasers using ray tracing simulation techniques

Matthias König

Master's Thesis

Aufgabensteller: Prof. Dr. C. Pflaum
Betreuer: 1.11.2021 – 2.5.2022
Bearbeitungszeitraum:

Abstract

This work showcases the application of ray tracing techniques for the calculation of absorption profiles in optically pumped solar lasers. It aims at using a lightweight and fast physically based raytracer combined with a biojective mesh adaptive direct search algorithm to optimize total power absorption and to minimize variance across the crystal. An exemplary setup of a side pumped Nd:YAG solar laser was simulated, optimized and the resulting beam quality evaluated.

Erklärung:

Ich versichere, dass ich die Arbeit ohne fremde Hilfe und ohne Benutzung anderer als der angegebenen Quellen angefertigt habe und dass die Arbeit in gleicher oder ähnlicher Form noch keiner anderen Prüfungsbehörde vorgelegen hat und von dieser als Teil einer Prüfungsleistung angenommen wurde. Alle Ausführungen, die wörtlich oder sinngemäß übernommen wurden, sind als solche gekennzeichnet.

Der Universität Erlangen-Nürnberg, vertreten durch den Lehrstuhl für Systemsimulation (Informatik 10), wird für Zwecke der Forschung und Lehre ein einfaches, kostenloses, zeitlich und örtlich unbeschränktes Nutzungsrecht an den Arbeitsergebnissen der Master's Thesis einschließlich etwaiger Schutzrechte und Urheberrechte eingeräumt.

Erlangen, den 27. April 2022

.....

Contents

| | | |
|----------|--|-----------|
| 1 | Introduction | 7 |
| 2 | Lasers | 8 |
| 2.1 | Stimulated Emission | 8 |
| 2.2 | Gain Medium and Population Inversion | 8 |
| 3 | Raytracing Framework | 10 |
| 3.1 | Raytracing Basics | 10 |
| 3.2 | Raytracing Acceleration | 14 |
| 3.3 | Sampling Techniques | 15 |
| 3.4 | Framework Structure | 17 |
| 3.4.1 | Rays | 19 |
| 3.4.2 | Shapes | 19 |
| 3.4.3 | Objects | 21 |
| 3.4.4 | Scene | 23 |
| 3.4.5 | Sampler | 25 |
| 3.4.6 | Utilities | 25 |
| 4 | Optimization | 29 |
| 4.1 | Optimization Methods Overview | 29 |
| 4.2 | Derivative-Free Optimization | 30 |
| 4.3 | Mesh Adaptive Direct Search (MADS) | 34 |
| 4.3.1 | Optimality and Clarke's Calculus for non-smooth Optimization | 34 |
| 4.3.2 | Constrained Optimization with the Barrier Approach | 36 |
| 4.3.3 | Mesh Generation and Execution of MADS algorithms | 36 |
| 4.4 | Biobjective MADS | 39 |
| 4.4.1 | Multiobjective Optimization | 39 |
| 4.4.2 | Pareto Dominance and Pareto Fronts | 39 |
| 4.4.3 | BiMADS | 41 |
| 4.5 | NOMAD Library | 43 |
| 5 | Optimization of Pump Light Absorption in a Nd:YAG Solar Laser | 44 |
| 5.1 | Setup and Simulation Parameters | 44 |
| 5.2 | Setup 1: Fixed Crystal Position and fixed Mirror Endpoints | 46 |
| 5.3 | Setup 2: Open Crystal Position and open Mirror Endpoints | 50 |
| 6 | Conclusion | 58 |

List of Figures

| | | |
|----|---|----|
| 1 | Ray-line intersection | 12 |
| 2 | Ray-AABB intersection | 13 |
| 3 | Subdivision using quadtrees | 15 |
| 4 | Uniform vs. stratified sampling | 16 |
| 5 | Inversion method for importance sampling | 17 |
| 6 | UML class diagram of the raytracing framework | 18 |
| 7 | UML class diagram of the Ray2D class | 19 |
| 8 | UML class diagram of the Shape2D and associated classes | 20 |
| 9 | UML class diagram of the Object2D and associated classes | 24 |
| 10 | UML class diagram of the Sampler and associated classes | 26 |
| 11 | Different examples of sampler output | 27 |
| 12 | Discontinuity and noisiness of the objective function | 31 |
| 13 | Example of GPS frames | 38 |
| 14 | Example of MADS frames | 39 |
| 15 | Pareto dominance | 40 |
| 16 | Pareto front | 41 |
| 17 | Example setup of the solar laser | 45 |
| 18 | VTK Output for Setup 1 with initial random search | 48 |
| 19 | VTK Output for Setup 1 with initial random search for different raytracing depths | 49 |
| 20 | ASLD beam profile for Setup 1 with initial random search | 50 |
| 21 | VTK Output for Setup 2 with initial random search | 52 |
| 22 | VTK Output for Setup 2 with initial random search for different raytracing depths | 53 |
| 23 | ASLD beam profile for Setup 2 with initial random search | 54 |
| 24 | VTK Output for Setup 2 with pipe start configuration | 55 |
| 25 | VTK Output for Setup 2 with pipe start configuration different raytracing depths | 56 |
| 26 | ASLD beam profile for Setup 2 with pipe start configuration | 57 |

List of Tables

| | | |
|---|---|----|
| 1 | Parameters for Setup 1 | 47 |
| 2 | Pareto optimal points for Setup 1 with initial random search | 48 |
| 3 | Parameters for Setup 2 | 51 |
| 4 | Pareto optimal points for Setup 2 with initial random search | 52 |
| 5 | Pareto optimal points for Setup 2 with initial pipe configuration | 54 |

1 Introduction

In the light of the recent developments in global energy policy, renewable energy has become one of the most important problems humanity has to solve. Ever new ways of exploiting the sun's vast amount of energy are becoming relevant if nations across the world want to achieve net-zero carbon emissions. One of those novel methods is the generation of hydrogen from water using solar energy. It can be achieved by common electrolysis or by reacting alkali metals with water. Researchers have been specifically looking at reacting magnesium (Mg) with water (H_2O) to produce hydrogen (H_2) and magnesium oxide (MgO) [10]. This reaction is exotherm and therefore causes a large amount of heat and produces hydrogen gas which could be stored in hydrogen fuel cells. Now if one can reduce the magnesium oxide to pure magnesium using the sun's energy one would have a solution to store solar energy using hydrogen. To drive the reduction of magnesium oxide a laser can be used but a considerable amount of energy is needed. In order to reduce losses that are induced by using a conventional solar panel that drives a diode to pump the laser, it could be beneficial to pump the laser crystal directly using sunlight. This is exactly what Shigeaki Uchida and his team in Japan have been researching [20] [21].

Another area of application that is becoming increasingly relevant is the usage of solar lasers in space exploration. Since there is no access to grid power in space and nuclear power is coupled with significant costs solar power is the most used source of power in space. The low efficiency of solar panels and the reduced number of parts of solar lasers make them an interesting prospect for usage in space. As mass is a high cost factor in space exploration the reduced weight and lower number of potential points of failure solar lasers could become a more relevant option in the future. The tasks of a solar laser in space could range from deep space communication, remote power transmission or tracking of objects.

Solar lasers require the collection of sunlight and focusing onto a gain medium to surpass the lasing threshold thereof. As it is the simplest and cost-effective method, usually a primary collector is used together with a secondary mirror in a two stage collector to focus the sunlight onto the gain medium [21]. The primary collector can be another mirror or a Fresnel lens as a cheaper alternative. The beam power and quality is significantly impacted by the amount of power absorbed by the gain medium and the uniformity of the absorption profile. The natural divergence of sunlight and dispersion effects in the Fresnel lens make it important that the secondary mirror is shaped in an optimal way. Both absorbed power and the uniformity of absorption need to be optimized. For the optical design of the collection system it is beneficial that the system is simulated accurately beforehand. For both the simulation and optimization part of the design process a free and open source framework was developed in this work in the hope that parts or the entirety of code may prove useful to engineers designing solar lasers. The goals of the framework are to offer a simple yet powerful interface for C++ applications. It provides a fast 2D raytracer for the calculation of the absorption profile in the gain medium which is then used by a mesh adaptive direct search algorithm in a biobjective manner (BiMADS) to increase both absorbed power and uniformity of the absorption profile. This is done via the open source library NOMAD version 3 [9], which implements the MADS [2] algorithm and a biobjective variant of it. It offers the efficient derivative free optimization of a black-box function with constraints.

The application of the framework is then demonstrated via an exemplary setup of a Nd:YAG solar laser using a two stage concentrator consisting of a Fresnel lens and a secondary mirror. In principle, any parameter of the setup can be optimized but for this example in particular the mirror shape is the interesting property. The result of the BiMADS algorithm is a Pareto front of optimal points determined by the algorithm. Depending on whether a more even distribution of power is desired or the total amount of power absorbed is relevant to the application, some points of the pareto front are then chosen and simulated with the software ASLD [17] to evaluate the resulting beam properties.

2 Lasers

Laser is an acronym which stands for Light Amplification by Stimulated Emission of Radiation. Lasers amplify coherent radiation at the infrared, visible, or ultraviolet part of the electromagnetic spectrum [16]. The principle was originally used in so-called masers the amplification of Microwave radiation or even radio frequencies. The advantages of using a laser system as a light source are that they produce a directional beam of coherent light which can be focused to a narrow spot [7]. Additionally, the emitted light is usually of a very narrow spectrum and thus reduces dispersion effects when shooting the beam through different media. Lasers are therefore used in a wide variety of applications which range from manufacturing processes to measuring systems to optical communication.

A laser usually consists of a gain medium that is capable of amplifying light that passes through by stimulated emission, a pump light to excite the atoms of the gain medium to higher quantum states and an optical feedback mechanism - often called cavity or oscillator - which usually consists of two mirrors that bounce the light back and forth through the gain medium [16]. One of those mirrors is only partially reflective and is transparent so that a portion of the amplified light can escape. Usually in more complex setups cooling is applied to the gain medium and some other optical elements like lenses or polarization filters may be present to ensure a better output beam quality. An ideal output beam is both temporally and spatially coherent, meaning that the emitted light is a perfect sine wave with constant amplitude and frequency and has a definite amplitude and phase pattern across any transverse plane inside the laser [16]. A measure for the quality of a laser beam is the M^2 factor, which is defined as in Eq. (1).

$$M^2 = \frac{\theta \pi w_0}{\lambda} \quad (1)$$

where θ is the beam divergence and $\frac{\lambda}{\pi}$ is the beam parameter product for a diffraction-limited Gaussian beam with the same wavelength [14]. w_0 is the beam radius at the waist of the beam. A perfect beam therefore has an M^2 factor of 1.

2.1 Stimulated Emission

There are three ways in which atoms exchange energy with a radiation field [7] identified by Albert Einstein. There is absorption where an electron is excited by a photon to a higher quantum energy state. Hereby the photon must have the exact amount of energy (wavelength) that the difference between energy state is. Then there is spontaneous emission where the excited electron jumps back to a lower energy state, emitting a photon in a random direction with a random phase shift but again with the same amount of energy as the difference between states of the electron. This can occur spontaneously at any time as the name suggests. The main principle why the gain medium amplifies light is the principle of stimulated emission. Electrons in the gain medium are stimulated by photons to a higher energy state. If now again photon with the same amount of energy and a certain direction hits the atom the electron jumps back to the lower state again emitting a photon of the same energy but crucially and contrary to spontaneous emission in the exact same direction and the exact amount of phase shift as the incoming photon. Therefore, amplifying the light by essentially "duplicating" the incoming photon.

Now if one wants a coherent output beam one needs to make sure that the photons are travelling only in one direction and with constant phase. This is the job of the resonator. It uses the photons from spontaneous emission which at some point will have the correct direction and bounce them between the mirrors. Photons with other directions will be lost from the sides entirely or will get absorbed again by the medium. Due to this process a majority of photons will be travelling in the desired direction after some time.

2.2 Gain Medium and Population Inversion

In order to be able to amplify the emitted light, more atoms in the gain medium have to be in an already excited higher state than in the lower state. Otherwise, "duplicated" photons will be

reabsorbed by atoms in lower state and will not be able to stimulate another emission or make it out of the laser cavity. Hence, the population of atoms needs to be inverted [7]. For this to happen an external source of energy needs to be supplied. This is called pumping and is usually achieved by a pump flash light or another laser. As it is equally likely that a photon causes stimulated emission or absorption there can not be only two states but at least three states are needed in optically pumped lasers [13]. The electrons are then excited into the highest state by the pump light from which they can decay into the middle state ready for stimulated emission. It is crucial for level three lasers that the pump light cannot push the electrons in the middle state back to ground state. This way it is possible to have more atoms in the middle state than in ground state and therefore population inversion is achieved. For this to happen the pump light intensity in level three lasers needs to be sufficiently high enough for the photons to be "ignored" by the electrons in the second state. The threshold for the pump power to achieve population inversion is called the *lasing threshold* and due to the energy levels in the atoms the choice of gain medium usually implies the choice of pump light or vice versa.

Materials that offer this property can be in gas, liquid or solid form. Solid form lasers are usually some sort of ion doped crystals or semiconductor diodes [7]. As an example for a three level gain medium ruby ($Cr^{3+} : Al_2O_3$) can be used. In practice mostly four level gain media are used as they offer a far lower lasing threshold for the pump power [13]. These are usually neodymium doped media like the most popular choice neodymium doped yttrium aluminum garnets (Nd:YAG).

3 Raytracing Framework

With the advent of cheap processors and increasingly powerful consumer hardware, ray tracing has become more popular in recent years. For the purpose of global illumination in video games and image processing, more advanced techniques have been continuously developed and improved. In optical design ray tracing is used to analyze the imaging quality of optical systems or as in this work other illumination properties can be simulated. The need for fast refresh rates in video games and the requirement of modelling more complex physical phenomena in optical design have led to tracing and sampling techniques that reduce the computational expense dramatically with minimal loss of accuracy. Focused on the specific problems of laser design, these improvements make it possible to get physically accurate results in an acceptable amount of computational time in an iterative context.

As in optical design systems are mostly rotationally symmetrical, the framework is meant to be used in a two-dimensional setup and calculated quantities, e.g. absorbed power in a medium converted to three-dimensional values after a simulation step. This significantly reduces the amount of rays needed to avoid undersampling effects and to produce stable results across multiple simulation runs. Intersection tests also require less computation and objects in the scene require less fundamental shapes to test a ray against. The resulting performance gains make it possible to run the simulation thousands of times in an iterative process to optimize some parameters in the optical setup even on consumer grade hardware. The objects in a scene are preprocessed to group fundamental shapes into leaves of a quadtree to reduce the amount of shapes a ray has to be tested against even further. To achieve the satisfied accuracy and to reduce noise the appropriate sampling strategies have to be used for a given problem. The most important techniques are provided including uniform sampling, stratified and importance sampling.

The framework was designed to provide a simple yet powerful interface for the user and was implemented in C++17. It provides the necessary data structures and algorithms for a fast raytracing solution. The sampling techniques are implemented in specialized classes of abstract interfaces. They can also be used by the user to implement custom techniques. The framework extensively relies on lambda functions to be provided by the user and thus naturally is customizable, although some preset functions are also provided. Because the calculations in the framework are so similar to applications in graphics software the OpenGL Mathematics header only library GLM [11] was used as an underlying maths library. GLM is based on the OpenGL Shading Language (GLSL) and so in a potential later step the framework could be ported to work on graphics cards providing that the data structures are changed to be accessible from a GPU. As in the specific problem in this work the tracing of each ray has side effects on the scene and on itself, i.e. the absorbed power of each ray has to be accumulated, it was decided to focus more on single core performance first and leave the parallel execution and execution on GPUs for a later point. Furthermore, IO utilities for simulations are provided for Comma Separated Values (CSV) files and structured output for the commonly used Visualization Toolkit (VTK) [15].

In the following chapters the applied ray tracing techniques explained in detail. Firstly the basics of raytracing, i.e. intersection tests of fundamental shapes and objects and reflection and refraction effects are shown. Then an applied method of subdivision for the performance optimization of the raytracer is explained. Lastly some methods of sampling are shown before the structure of the developed framework is presented with code samples. Here the usage of classes is demonstrated, and it is shown how specific objects are defined. In particular the objects which are relevant for the simulation of laser cavities and which are used in the example setup are shown.

3.1 Raytracing Basics

The techniques presented in this chapter are largely explained in the excellent lecture *Global Illumination* by Stamminger at FAU [19]. While the lecture applies those techniques in a different context, namely for the purpose of generating physically accurate images in image processing applications or video games, a selection of the techniques are still relevant to using ray tracing in scientific computing. Since the aim of both fields is slightly different, the priorities shift regarding computational performance or numerical accuracy. In scientific computing more focus is laid on

the accurate modelling of physical phenomena. For example, while in image processing it is sufficient to use a faster approximation of Snell's law in Eq. (8) in application of physical raytracing one might rather evaluate the actual law and take the additional computational cost of evaluating trigonometric functions into account. Nevertheless, there is a large overlap between the two fields of application and a lot of techniques are entirely applicable in scientific computing as is.

Rays are represented as a parametric line from a ray origin \mathbf{o} in direction \mathbf{d} . The parameter t goes is in the interval $[0, \infty)$ and represents the closeness of the ray to the origin. The mathematical representation therefore is given as

$$\mathbf{r}(t) = \mathbf{o} + t\mathbf{d} \quad (2)$$

After the ray is generated it is tested against intersections with the scene. Here the smallest $t > 0$ of all the intersections with objects has to be found. The question if a ray intersects an object can usually only be answered for simple fundamental shapes, e.g. lines, circles, axis aligned bounding boxes (AABBs) in 2D or planes, triangles, spheres, etc. in 3D. Therefore, objects are normally comprised of a collection of fundamental shapes and an intersection occurs if one of the fundamental shapes is intersected. Naturally, an object can be intersected multiple times by the same ray and so the results have to be searched for the smallest t . Each fundamental shape should be represented in a parametrized form, so the intersection test can be represented as a system of equations. The two fundamental shapes used in this work are 2D lines and axis aligned bounding boxes (AABBs).

Lines are represented by two points \mathbf{a} and \mathbf{b} . So the intersection problem can be written as a ray-ray intersection as follows:

Find $\alpha \in [0, 1]$ and $t \in [0, \infty]$ s.t.

$$\mathbf{a} + \alpha(\mathbf{b} - \mathbf{a}) = \mathbf{o} + t\mathbf{d} \quad (3)$$

If such a combination of α and t exists, we have an intersection. As we are in 2D there are two equations for two unknowns and the system always has a solution. The solution can then be checked, s.t. the values are in the right intervals. A small mathematical trick is to define a 2D cross product which is basically just the z component of a 3D cross product if the two input vectors \mathbf{p} and \mathbf{q} were parallel to the xy plane:

$$\mathbf{p} \times \mathbf{q} = p_x \cdot q_y - p_y \cdot q_x \in \mathbb{R} \quad (4)$$

Observe that same as the 3D cross product, the 2D version becomes 0 when you cross a vector with itself. If one now crosses Eq. (3) with \mathbf{d} on both sides the intersection equation becomes:

$$\mathbf{a} \times \mathbf{d} + \alpha(\mathbf{b} - \mathbf{a}) \times \mathbf{d} = \mathbf{o} \times \mathbf{d} \quad (5)$$

So t has been eliminated from the equation and we can solve Eq. (5) for α :

$$\alpha = \frac{(\mathbf{a} - \mathbf{o}) \times \mathbf{d}}{\mathbf{d} \times (\mathbf{b} - \mathbf{a})} \quad (6)$$

If α satisfies the condition, we continue analogously for t by crossing Eq. (3) with $\mathbf{b} - \mathbf{a}$. The resulting t is then checked against the condition and a normal at the intersection point is calculated. The intersected rays can be seen in Figure 1.

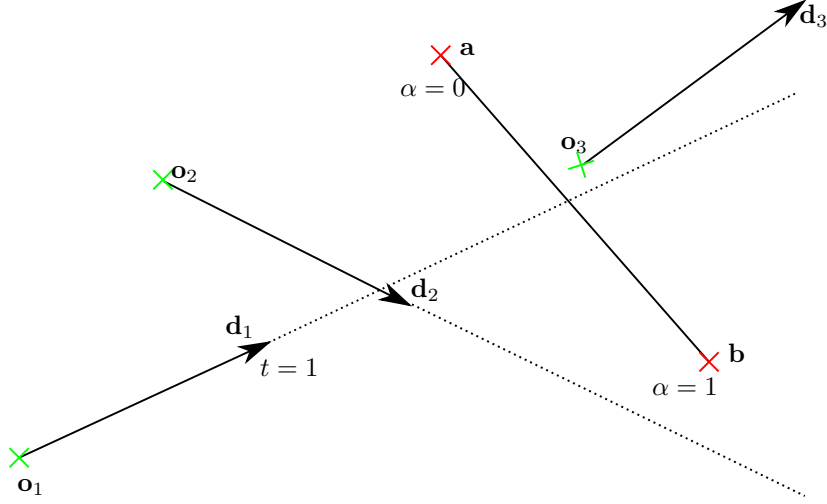


Figure 1: Ray-line intersection of two rays. The line is specified by the points **a** and **b** and the rays are defined by the origins \mathbf{o}_i and directions \mathbf{d}_i . Ray $(\mathbf{o}_1, \mathbf{d}_1)$ satisfies the conditions $t \geq 0$ and $0 \leq \alpha \leq 1$ and therefore causes an intersection, ray $(\mathbf{o}_2, \mathbf{d}_2)$ dissatisfies the α condition and ray $(\mathbf{o}_3, \mathbf{d}_3)$ does not satisfy the t condition.

Another important shape to intersect are AABBs. They are rectangles aligned with the axis of the coordinate system, so they require minimal memory space and intersection tests are as simple as possible. They most often used to surround complex objects or parts of it to reduce the amount of intersection tests. First the AABB of the object is tested and only if there is an intersection the actual fundamental shapes inside the AABB are tested. A 2D AABB is defined by two points \mathbf{b}_{min} and \mathbf{b}_{max} which represent the lower left and upper right corner of the rectangle. The intersection test is done by comparing the values of t at each of the axis aligned lines defining the box. The t values for the x axis aligned lines can be calculated as shown in Algorithm 1.

Algorithm 1: Intersection test for a AABB $(\mathbf{b}_{min}, \mathbf{b}_{max})$ with ray (\mathbf{o}, \mathbf{d})

```

 $t_{x1} = \frac{b_{minx} - o_x}{d_x};$ 
 $t_{x2} = \frac{b_{maxx} - o_x}{d_x};$ 
 $t_{min} = \min(t_{x1}, t_{x2});$ 
 $t_{max} = \max(t_{x1}, t_{x2});$ 
 $t_{y1} = \frac{b_{miny} - o_y}{d_y};$ 
 $t_{y2} = \frac{b_{maxy} - o_y}{d_y};$ 
 $t_{min} = \max(t_{min}, \min(t_{y1}, t_{y2}));$ 
 $t_{max} = \min(t_{max}, \max(t_{x1}, t_{x2}));$ 
if  $t_{min} \geq 0$  and  $t_{min} \leq t_{max}$  then
  | AABB was hit!
end

```

If the conditions $t_{min} \leq t_{max}$ and $t_{min} \geq 0$ hold there is an intersection. This process is better understood visually and is illustrated in Figure 2. If normals are needed they can be easily calculated since there are only four possibilities depending on which side of the box is intersected first.

The AABB intersection becomes really handy once one wants to use them for ray tracing acceleration techniques, as they can easily be constructed to surround a cloud of points and then be used as a spacial subdivider in a tree structure. This is described in detail in the next chapter. Other shapes like circles or ellipses are intersected in a similar way but as they are not used in the example below the intersection process is not explained here.

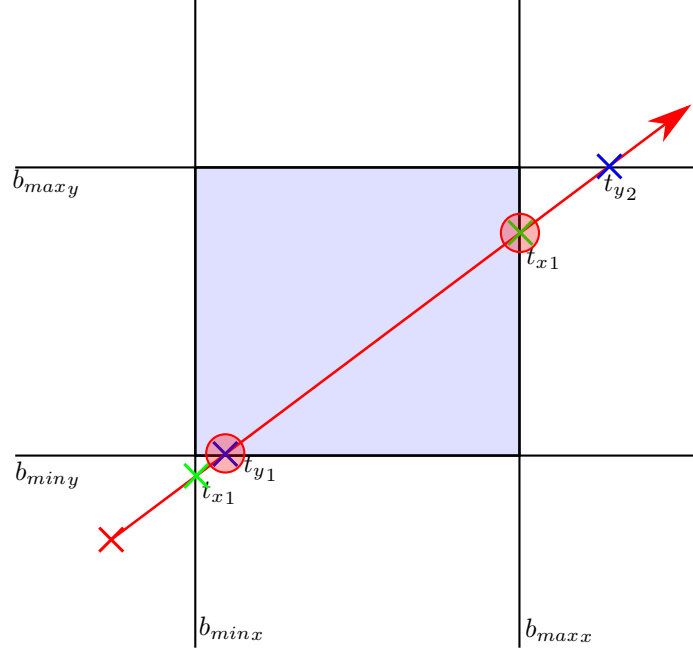


Figure 2: Ray-AABB intersection, where first the intersection points with the x axis (marked in green) and y axis (marked in blue) are calculated. Each of the values t_{i1}, t_{i2} are then split into the minimum and the maximum of the two. Both maximums are then compared and the minimum is chosen as the final t_{max} . Analogously the minimums are compared and the maximum is chosen as t_{min} (marked with red circles). Thus there is an intersection with an entry point $\mathbf{o} + t_{min}\mathbf{d}$ and an exit point $\mathbf{o} + t_{max}\mathbf{d}$ and the normals can be calculated depending on which sides the points reside.

Once an intersection takes place, the ray will be either reflected, terminated or refraction occurs depending on the desired material of the object. Total reflection is only dependent on the incident angle θ_i to the normal of the surface at the hitpoint. Then the reflection angle θ_r is given by Eq. (7).

$$\theta_r = -\theta_i \quad (7)$$

A new ray is then generated at the hitpoint pointing in the direction given by θ_r . Due to limited floating point precision, it is required that the origin of the new ray is shifted by a small ϵ towards the reflection direction in order to make sure the ray is originated at the correct side of the material. Since the reflection is total the entire amount of power of the incident ray is transferred to the reflected ray.

When hitting a material that is transmissible for light the ray will be refracted at the boundary between the two media. The effects of matter on a light beam are described by Snell's law and the Fresnel equations. The ray is split into a reflected and a transmitted ray. The direction of the transmitted ray is governed by Snell's law in Eq. (8) which depends on the indices of refraction of the two media n_i and n_t .

$$n_i \sin(\theta_i) = n_t \sin(\theta_t) \quad (8)$$

Usually one rearranges the Eq. (8) in order to solve for θ_t .

$$\theta_t = \text{asin}\left(\frac{n_i}{n_t} \sin(\theta_i)\right) \quad (9)$$

Arranged like in Eq. (9) one can observe that if $\frac{n_i}{n_t} > 1$ the argument of the asin function can also be greater than 1 depending on the incident angle θ_i . In this case the arcussinus is undefined and

therefore Snell's law does not hold. But rather than presenting a mathematical problem this only models what happens in reality. If for instance a light ray transitions from a medium of higher refractive index n_i to a medium with lower refractive index n_t and the angle of incidence θ_i is low enough for the expression $\frac{n_i}{n_t} \sin(\theta_i)$ to become greater than one, the light is no longer transmitted to the medium with lower refractive index. Instead, the entirety of the light ray is reflected back to the medium with higher refractive index. This phenomenon is called total internal reflection and is an effect that is abused in many physical applications, e.g. fiber optics communication. The light can travel along an optical fiber and even bends in the fiber because the material has high enough refractive index and the angle of light hitting the inside border from the fiber to air or other materials is low enough. In such scenarios the critical angle below which total internal reflection occurs is then given by $\theta_{crit} = \text{asin}\left(\frac{n_t}{n_i}\right)$. An implementation of Snell's law therefore needs to detect, when total internal reflection takes place. Naturally, the reflected ray is still reflected as given in Eq. (7). The transmitted and reflected power can be calculated with the transmission- and reflection rates given by Fresnel's equations. These are dependent on the orientation of the polarization of the incident ray (perpendicular or parallel) to the surface.

$$R_{\perp} = \frac{\sin^2(\theta_1 - \theta_2)}{\sin^2(\theta_1 + \theta_2)} \quad R_{\parallel} = \frac{\tan^2(\theta_1 - \theta_2)}{\tan^2(\theta_1 + \theta_2)} \quad T_{\perp} = 1 - R_{\perp} \quad T_{\parallel} = 1 - R_{\parallel} \quad (10)$$

For unpolarized light the total rates are just given by the average.

$$R_{total} = \frac{R_{\perp} + R_{\parallel}}{2} \quad T_{total} = \frac{T_{\perp} + T_{\parallel}}{2} \quad (11)$$

An additional effect that can be significant especially for broadband applications is the dependency of the index of refraction of a medium on the wavelength of the light passing through and the dispersion of light resulting from this. This is modelled by the Sellmeier equation, which is based on empirical measurements. The relationship between the refractive index n and the wavelength λ in micrometers is described by a series of Sellmeier coefficients B_i and C_i that have been determined by experiment. The Sellmeier equation is thus given by Eq. (12).

$$n^2(\lambda) = 1 + \sum_i \frac{B_i \lambda^2}{\lambda^2 - C_i} \quad (12)$$

3.2 Raytracing Acceleration

As the raytracer is later intended to be used in an iterative optimization algorithm, it is of vital importance that unnecessary computational cost is avoided. For a raytracer this can be achieved in a number of ways. The first and simplest way is to simply reorder the objects in a scene by a heuristic that describes the likelihood of an object to be the first object hit by the majority of the rays. Of course, this only works well if rays are shot into a scene from a dominant direction. Another way would be to subdivide the entire 2D scene with quadrees and try to fill each branch of the tree with an equal amount of objects or shapes.

Similarly, one can also subdivide an object itself and sort the fundamental shapes comprising that object into a quadtree. This method was chosen in this work as there are a limited amount of objects in the scene with the objects possibly being quite complex. Once the fundamental shapes of an object are known, they can be sorted into a quadtree of AABBs of a chosen depth. The outermost AABB is the root of the tree with four children, each encompassing the shapes inside their quarter of space as tightly as possible. This is recursively done until the desired depth is hit. The intersection test of an object then can be done by hitting the root AABB of the tree and then stepping through its children via breadth first search. Each AABB child the ray hits, is pursued further and the ones the ray doesn't intersect are ignored. If a leaf has been hit all the shapes inside are then tested for intersection. Finally, the t values of all the intersections are compared and the minimum and the maximum chosen as entry and exit points. The advantage of this is that AABB intersection tests are done really fast and a large number of fundamental shape intersection

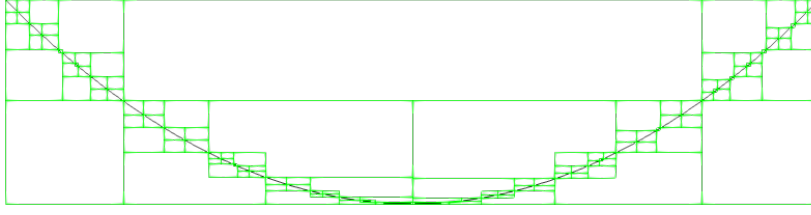


Figure 3: A parabolic mirror comprised of line segments subdivided by a quadtree of AABBs with depth 4. Note that the AABBs are encompassing their contained line segments as tightly as possible.

tests are avoided. An illustration of subdivision of a mirror comprised of line segments is given in Figure 3 and the intersecting algorithm for a single object is given in Algorithm 2.

Algorithm 2: [Object intersection]Intersection test for a single object subdivided by a quadtree

```

IntersectionResult objectResult;
objectResult.tEnter = MaxFloatingPoint;
objectResult.tLeave = MinFloatingPoint;
Queue treeQueue;
treeQueue.push(object.root);
while !treeQueue.empty() do
    tree = treeQueue.front();
    IntersectionResult aabbResult = tree.aabb.intersect(ray);
    if aabbResult.hit then
        for shapes in tree.shapes do
            IntersectionResult shapeResult = shape.intersect(ray);
            if shapeResult.hit then
                | set objectResult appropriately;
            end
        end
        treeQueue.push(tree.children);
    end
    treeQueue.pop();
end

```

3.3 Sampling Techniques

The accuracy and performance of ray tracing simulations are heavily dependent upon using the correct sampling techniques. One could sample values on a uniform grid or equally spaced intervals. The problem with this is that there is no randomness or irregularity causing structured aliasing errors in most applications. Random sampling however always relies on some sort of random number generation. These are usually pseudo random numbers generated according to some distribution with the generation engine initialized with a seed. Usually when one samples according to some scheme only values in $[0, 1]$ are allowed. The returned sample is then later scaled to the desired range depending on the usecase. It is also to be noted that calls to a sampler must be ensured to be as efficient as possible as a large number of calls will be made during the simulation.

The simplest sampling scheme is uniform sampling. It returns values uniformly and can be implemented right on top of the random number engine of the used system. The advantage of uniform

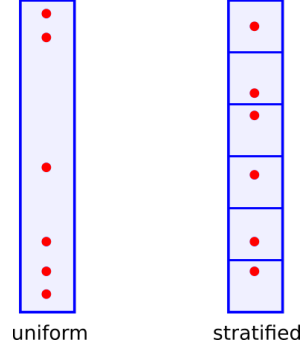


Figure 4: Uniform sampling of a 1D interval (left) vs. stratified sampling (right). Observe the large gap between samples on the left whereas the samples on the right are spaced out more equally.

sampling is that it produces close to random samples without the need for additional logic and therefore performance losses. The disadvantage is the irregular density of samples within the interval. There can be areas with a lot of samples and large gaps between. So in scenarios where there needs to be a more regular distribution of samples uniform sampling is not optimal.

For this reason another sampling technique called stratified uniform sampling exists. Here the domain is split into N equally spaced intervals and the uniform sampling occurs within each interval. This ensures that there is some amount of regularity while still keeping the randomness of uniform sampling. An application of stratified sampling would be the definition of a light source in the simulation. The direction or origin of the rays the light source emits can be sampled according to stratified sampling to ensure a smooth illumination of the scene. The difference between uniform and stratified uniform sampling can be observed in Figure 4.

A more advanced technique is to sample values where they are contributing the most. Suppose one wants to approximate some function f over a domain $[0, 1]$. The criterium that has to be met in order to calculate some quantity Q is given by any arbitrary integral in the domain. With uniform sampling of $x \in [x_1, x_2]$ by the sequence (x_i) and $i = 1 \dots n$ the integral is approximated by Eq. (13).

$$Q = \int_{x_1}^{x_2} f(x) dx \approx \frac{1}{n} \sum_{i=1 \dots n} f(x_i) \quad (13)$$

Now it is also possible to sample according to some other distribution. One just has to know the probability density function (pdf) p to know how likely it is that a sample x_i is generated. Probability density functions are non-negative across the domain and their integral over the domain is always 1. This corresponds to the probability that a sampled value is in the interval $[x_1, x_2]$ which is of course the case when all possible values are within that interval. The more accurately the pdf p matches f the more $[x_1, x_2]$ is sampled at the points where the function f has a large contribution to the integral. This can significantly reduce the amount of samples needed to get an accurate approximation for the integral Q . The integral is then approximated by Eq. (14).

$$Q = \int_{x_1}^{x_2} f(x) dx \approx \frac{1}{n} \sum_{i=1 \dots n} \frac{f(x_i)}{p(x_i)} \quad (14)$$

Observe that now the values for f are weighted by the likelihood p . If it is likely that a sample x_i is generated - larger p - then the contribution is worth less and vice versa. Of course this requires some preprocessing in order to generate the distribution P from a pdf p . Usually one wants to generate p from f , but there are also cases where one might choose another function to deduce the pdf and subsequently the distribution.

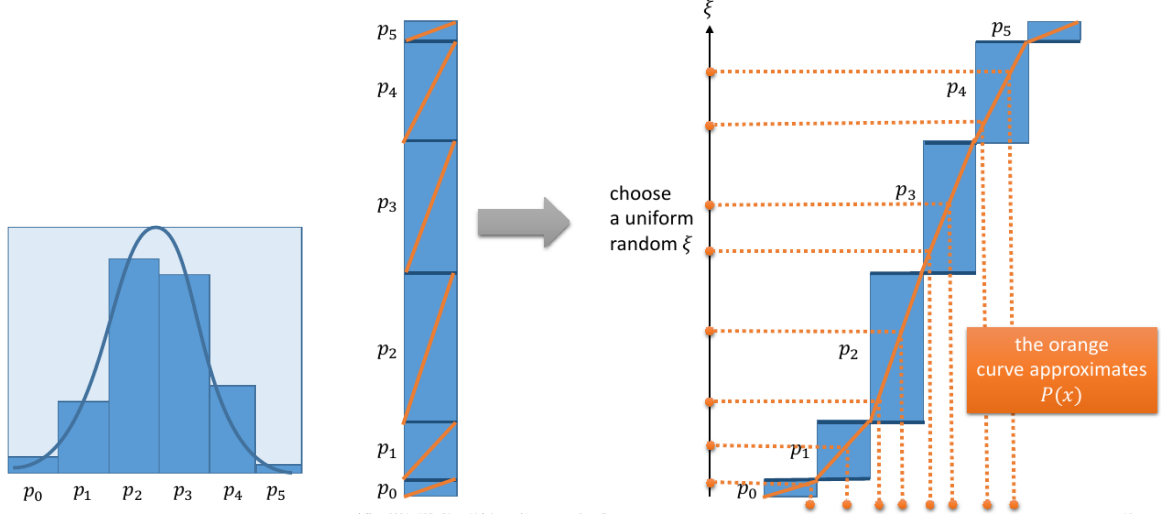


Figure 5: Visualization of inversion method to sample according the pdf on the left. The intervals p_i are summed up and stacked. Then a $\xi \in [0, 1]$ is uniformly sampled and the corresponding interval is searched. The returned value is interpolated linearly according to the value of ξ within the rectangle.

One method of building such a distribution is to first integrate f in the domain $[x_1, x_2]$ and normalize the function, so the integral is guaranteed to be 1. Then to sample according to the resulting pdf one discretizes the pdf to a finite amount of equidistant intervals $p_i = [x_{1i}, x_{2i}]$. For an interval p_j the values $p(x_{2i})$ for all $i < j$ are then summed up progressively assigned to that interval. These resulting rectangles are then stacked so that each rectangle represents an interval in x and the corresponding values of the sum of the pdf. Then a sample $\xi \in [0, 1]$ is drawn from a uniform sampler and the corresponding interval in which the value ξ lies in is searched in the list of intervals using binary search. Once the interval is found we interpolate linearly between the lower boundary x_{1i} and x_{2i} depending on ξ . Then the resulting $x \in [x_{1i}, x_{2i}]$ is returned along the value of the pdf $p(x)$ as a sample. This process approximates the distribution P and is called the inversion method. It is better understood when visualized as in Figure 5.

3.4 Framework Structure

The goal of the raytracing framework is to offer a free and lightweight alternative to commercial raytracers in order to stay efficient for the later usage in a black-box optimization context. For the optimization, it is crucial that the raytracer can be executed thousands of times even with a higher number of rays without significant overhead. It is to be noted that the raytracer has been specifically designed in order to be used in the optimization of geometrical parameters in rotationally symmetrical systems. Therefore, the decision was made to work in a 2D context rather than a 3D one. The additional computational cost of going from a 2D to a 3D context for raytracing is significant and since the framework is to be used as the optimization part of the design process the results can then be taken and further analyzed in a 3D raytracer. Suppose a 2D raytracer needs 10000 rays to reduce the noise to a satisfactory level. Then it can be assumed that a 3D raytracer needs about $10000 \cdot 10000$ rays to produce the same result. The only difference is that transversal rays cannot be modelled in 2D but transversal rays which may occur by divergence of sunlight or scattering effects in unpure media are statistically distributed equally across the full rotation of a rotationally symmetrical system and the impact on the result is therefore negligible. Additionally, the described objects in the scene require a significantly higher amount of fundamental shapes, which compounds the performance loss of needing more rays even further. Furthermore, the ray intersect equations shown above would become more complex and would require more arithmetic and cases. So for the relatively small benefit of being able to model transversal rays it is infeasible

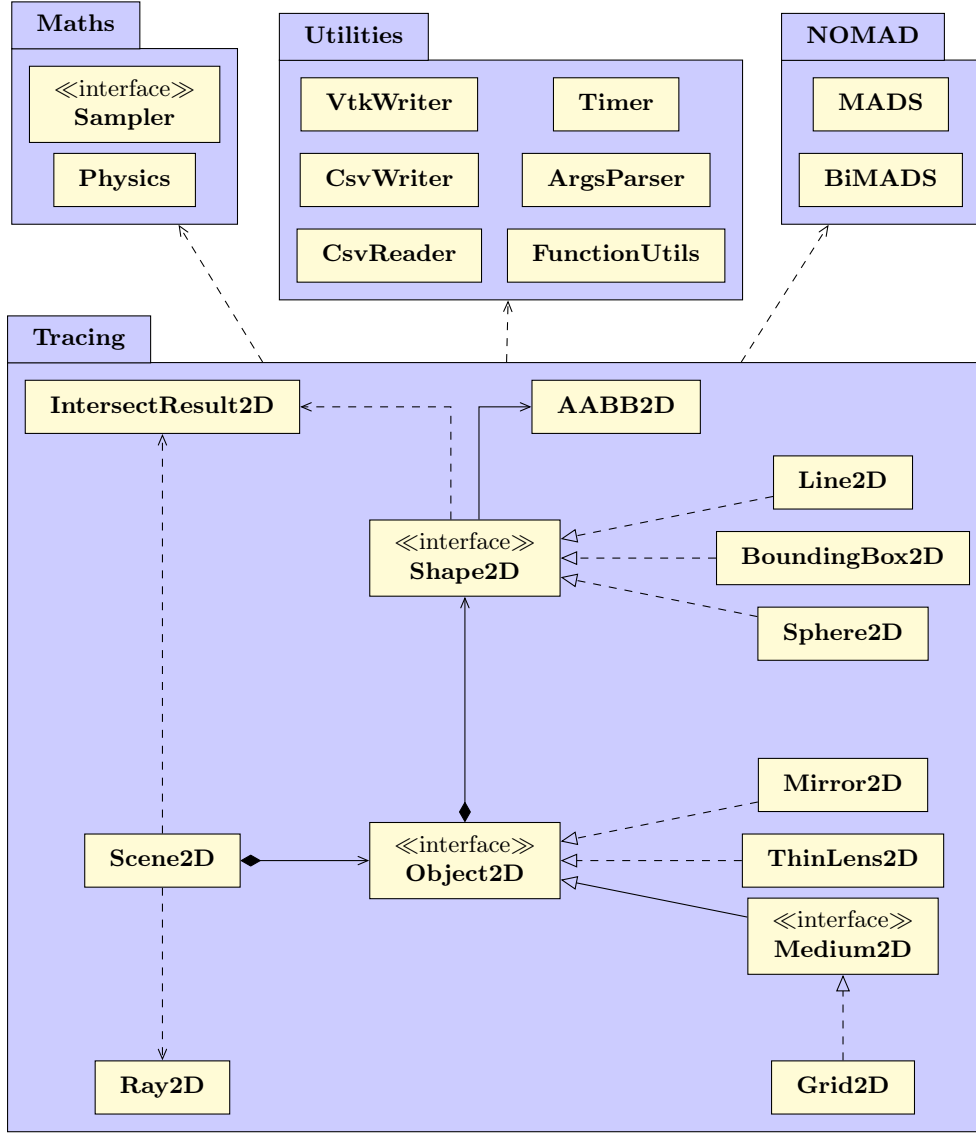


Figure 6: UML class diagram of the raytracing framework

in a rotationally symmetrical system to simulate in a 3D environment. Of course, if the system is not rotationally symmetrical then there is no other choice than to trace the scene in 3D, but this is not the norm in laser optical systems. In the following chapter the most important parts of the raytracer framework are presented. The datastructures and algorithms are shown in an UML class diagram and an example application of the datastructure or algorithm is given. It is to be noted that not all fields, methods or datatypes are shown in the UML diagrams and the code should therefore be seen as pseudocode instead of specific C++ code. When the classes have already been explained and the fields are not necessary to understand the relation between them, they are omitted from the diagram to keep the diagrams more manageable. The *float* datatype represents some floating point datatype and not necessarily the C++ datatype. The *vec** vector datatypes are either the GLM [11] datatypes for vectors - if the dimension is 4 or below - or a custom implementation to mimic the vector arithmetic of GLM for higher dimensions. Pointer datatypes in the UML diagrams are entirely reliant on the STL smart pointers in C++. Thus, the user usually constructs instances of the objects or shapes via smart pointers which implement reference counting in order to manage heap allocated resources. Therefore, there is no need for the user to worry about memory management. Before going into more detail for each part of the raytracing framework a rough overview over the structure and different components is given in Figure 6.

| Ray2D |
|---|
| + origin : vec2 + direction : vec2 + power : float + wavelength : float + terminated : bool + terminatedAt : float |
| + terminate(t : float) : void + reflect(t : float, normal : vec2) : Ray2D + refract(t : float, normal : vec2, n_1 : float, n_2 : float) : tuple<Ray2D, Ray2D> |

Figure 7: UML class diagram of the Ray2D class

3.4.1 Rays

Rays are the most basic datastructure in the simulation. They are described by an origin, a direction, a field for the amount of power, wavelength and a bool field if a ray has already been terminated. The simplest action is to just terminate the ray at some t in which case it will no longer be considered in the tracing algorithm. Rays can also be reflected at a point t with a certain normal, where the original ray is terminated and a new ray according to Eq. (7) with a small ϵ shift for the origin in the reflected direction is returned. Another action is to refract the ray between the boundary of two media with refractive indices n_1 and n_2 . Here a tuple of new rays is returned, and the original ray is terminated. The first element is the reflected ray and the second element is the transmitted ray into the medium. The direction of the transmitted ray is calculated using Eq. (8). It should be noted here that as explained in Section 3.1 there does not necessarily exist a transmitted part of the ray. This is due to the phenomenon of total internal reflection which can occur once the ray transitions from a medium with high reflective index to a medium with low refractive index. In such cases the implementation of the *refract* method detects that Snell's law is undefined and reflects the ray with the entire amount of power back into the medium. In the normal case the power of the original ray is split between the reflected and transmitted part according to the Fresnel laws Eq. (10) for unpolarized light Eq. (11). The UML class diagram for the Ray2D class and other relevant classes is shown in Figure 7.

As the user rarely has to interact directly with ray class and the implementation and usage of the methods are straight forward an example is not necessary here.

3.4.2 Shapes

The Shape2D class represents all fundamental shapes in two dimensions It is the baseclass for all specific 2D shapes like lines, AABBs or circles etc. The specific intersection tests with rays are implemented in those derived classes. Each shape additionally has an AABB that encompasses the represented shape. This AABB is then used to construct the quadtree for the object the shape is part of. When a shape is intersected an intersection result is returned, which contains the enter and leave t value of the intersection and a boolean that represents whether an intersection has even occurred. Furthermore, the normals at the enter and leave point are contained in the intersection result. Each shape also has a line representation in order to later output the scene in the VTK format for visualization. A UML class diagram of the Shape2D class is shown in Figure 8.

The shapes that are derived from the Shape2D class are the basic unit for the intersection tests used in the tracing algorithm. The implementation of those tests should therefore be computationally efficient and should avoid unnecessary branches. Ideally they should be branchless implementations where only the final decision if an intersection has occurred requires a branch. An example for a

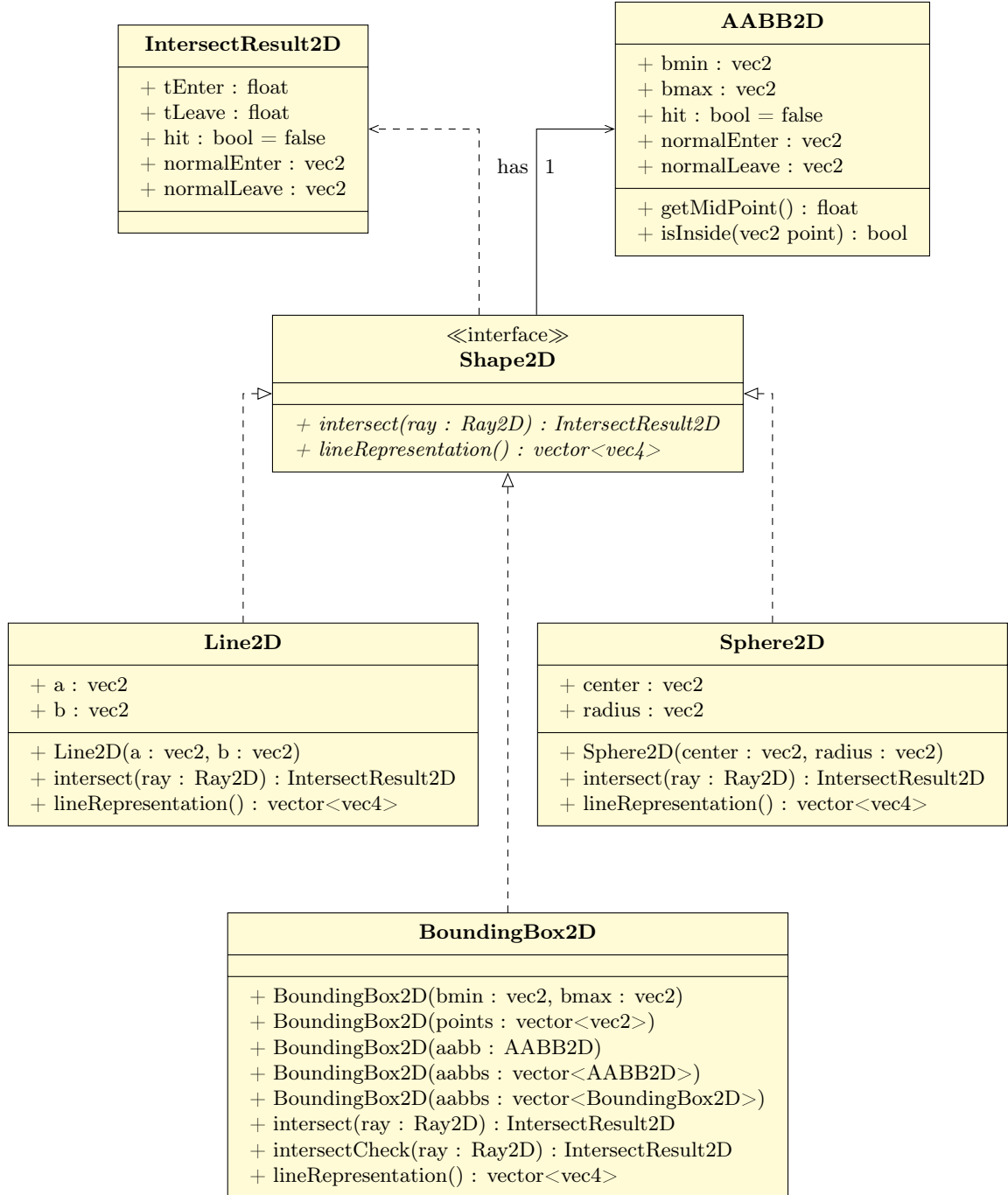


Figure 8: UML class diagram of the Shape2D and associated classes

branchless intersection test has been shown in Section 3.1 above, specifically the ray-AABB and ray-line intersections. For the ray-AABB intersection two versions of the test should exist. One version that only checks for the intersection and one version, which also calculates the normals. The check-only variant should then be used in Algorithm 2 as no normals are needed to traverse the quadtree and the AABB normal calculation is quite branch heavy. This is what the *intersectCheck* method of the BoundingBox2D class is for. Furthermore the BoundingBox2D class provides multiple ways of constructing the represented AABB. Either directly by giving b_{min} and b_{max} or by providing a point cloud or by merging multiple AABBs together. This is then later used in the construction of the quadtree of the object the shape is in.

3.4.3 Objects

Objects are represented by the Object2D class and are essentially a collection of Shape2D instances. Similarly to the Shape2D class the Object2D is just the base class for the specific objects implemented by the user or predefined by the framework. To initialize an object a list of shapes has to be provided. The constructor of the Object2D class then builds the quadtree of shapes from that list as described in Section 3.2. The intersection test for the object is then done as shown in Algorithm 2. Furthermore, the object base class provides a virtual method for a user defined action to be executed once a ray hits the object. A few presets are already implemented namely pass, absorb and reflect. Pass just ignores the object entirely, absorb terminates the ray at the entry point of the intersection and reflects the ray at the hitpoint. The user defined action provides the capability for the framework to be extensible and customizable. It provides the ray, the intersection result and a reference to a list of newly created rays for the user. For example, the ray could hit the surface and spawn multiple new rays instead of just being reflected modelling some sort of scattering effect. This isn't implemented by the framework out of the box, but the user can easily implement this functionality in a single function. The Object2D class therefore is intended to provide the bare-bones functionality for efficient tracing of an object, but the actual physical modelling of the interaction of a light ray with the object can be entirely customized by the user.

Objects that are arbitrarily complex can thus be efficiently implemented with minimal programming. Examples of how the usage of the Object2D class is intended can be seen in the paragraphs below. Here a thin lens approximation, a reflective mirror, and a grid representing a laser crystal are implemented and can be used by the user. A UML class diagram of the Object2D class and associated classes is given in Figure 9.

Medium2D All object that consist of some material that is transmissible by light and have a non negligible thickness should implement the Medium2D interface. It holds information about the material via the materials Sellmeier coefficients and implements the all the phenomena relevant to the correct tracing of light on the border between two materials of different refractive index. These are Snell's law in Eq. (8) for the bending of the ray on material boundaries, the Fresnel laws in Eq. (10) for the correct amount of intensity to be transmitted or reflected and the Sellmeier equation of the lens material in Eq. (12) to accurately describe dispersion effects of the material.

Like all objects in the simulation it inherits from the Object2D class and implements the *action* method in to include the above described effects. Furthermore, the Medium2D class provides the abstract *actionEnter* and *actionTransmit* methods which are executed once the ray first hits the medium and once the transmitted part of the ray was traced within the medium respectively. They can then be implemented by the user in a user defined object implementing the Medium2D interface. These actions can even modify the affected light ray in order to model absorption or thermal lensing effects within the medium. If the ray is terminated by the user in the *actionTransmit* function, no further tracing is done and no additional rays are created. An example of this modification to the ray itself by the user is the Grid2D class. Here the power of the ray is modified by each cell the ray intersects in order to model the absorption of light within a medium.

The Medium2D interface should serve as the base class for all user defined objects where the tracing of light needs to be physically accurate. This means that no approximations are made and the required computation per ray transmitting through these objects is quite high. Additionally, one ray that hits the object then in turn creates three rays only one of which - the ray within

the medium - is always guaranteed to be terminated. The other two generated rays, namely the reflected part and the ray exiting the medium on the other side are two completely new rays entering the scene. These rays then need to be traced, increasing the overhead of tracing a medium accurately even more. Therefore, it is advised to use the Medium2D interface with great care and sparingly in order to keep the computational cost to a minimum. Only the most relevant objects to the simulation should be traced with full physical accuracy. Suppose one wants to model a mirror using the Medium2D class. Technically this is possible, but practically it is infeasible, since the only thing the user is most likely interested in is the reflected part of the incoming ray. The same is true for lenses or optical elements where either the dispersion effects are negligible or the angle of incidence is such that almost all light is transmitted anyway. In this case the user is most likely only interested in the transmitted part of the ray and not the reflected or internal part. To prevent this unnecessary computational cost, one usually wants to approximate or neglect certain parts of the tracing in media. This is what the ThinLens2D and Mirror2D classes shown below demonstrate.

ThinLens2D The accurate physical simulation of a lens follows the same laws as the ray tracing in all media. This is modelled by the Medium2D interface, which implement all relevant effects in a transmissible material. Although it is physically accurate to trace the light rays with the Medium2D class, significant amounts of computation is needed to calculate and describe the light paths. Furthermore, the geometry of the lens needs to be modelled accurately. This is simple for conventional glass lenses where the geometry can be described only by the radii of the surfaces and the thickness of the lens. But for Fresnel lenses this process can be quite complex and time-consuming, both in the modelling phase and the computational cost of tracing many fundamental shapes. Thus it is rarely feasible to trace lenses without any amount of simplification. The question of choosing the appropriate amount of approximation depends on the goal of the simulation and the use case of the optical system and cannot be generally answered. It can be required to trace a specific lens with all the effects described above if the goal of the simulation is to design that specific lens for example. For imaging systems like camera objectives, the lenses are usually aligned in their optical axis, rays are predominantly entering the system at shallow angles and dispersion effects can be largely neglected. Other tasks may require rays to hit the lens at odd angles, so the correct geometry of refraction is important, but dispersion effects and transmitted power are not that important or can be approximated by another way. Therefore, the user ultimately needs to decide which amount of approximation is acceptable for the task at hand.

Suppose the user simulates a camera objective. Like in most optical systems a larger number of lenses are aligned in their optical axis and rays are only hitting the lens with a small angle with respect to those axis. Here, the only thing that matters is the correct refraction of rays according to the rules of geometric ray tracing in a thin lens. Parallel rays always intersect the focal point and rays that travel through the middle of the lens will not be refracted at all. Those lenses are therefore often modelled by the ABCD ray transfer matrix [12]. The lens is seen as a sort of black-box with a certain thickness and the transfer matrix describes how a ray is transmitted through the lens. The only information needed is the thickness of the lens and the focal point of the lens. If multiple lenses are in a row and described by ABCD transfer matrices, the transfer matrix of the whole system can then be calculated from the individual ones. The ABCD transfer matrix only provides correct results once the angles of the ray with respect to the optical axis of the lens are shallow. Then the $\sin(\theta)$ in Snell's law Eq. (8) is just approximated by θ for small angles (paraxial approximation).

Since lenses in the raytracer in this work can be rotated in any way, a more general approach is to solve a trigonometrical formula for each ray hitting the lens. In this case also rays with steep angles are refracted correctly. For the purposes of simplification the lens is usually made infinitely thin. This way of tracing a thin lens is described in [5]. It provides a good compromise between an approximation and using fully accurate refraction on a exactly modelled piece of glass, where normals and angles need to be calculated and the laws of Snell, Fresnel and Sellmeier need to be applied. Naturally, dispersion effects can not be modelled by this approach, but for non-imaging systems it is often sufficient to trace lenses without dispersion effects, especially because glass has a very low dependency of the refractive index on wavelength according to its Sellmeier coefficients. If one still wants to model dispersion effects with this approach, one method could be to provide

an artificial thickness function or just upper bound depending on the application’s requirement for physical accuracy. Then the Sellmeier coefficients for the desired material of the lens in combination with the sampled thickness at the hitpoint can be used to disperse the ray correctly. An example for this would be a Fresnel lens made from PMMA. The sawtooth pattern of the ridges could then be given as a function to be sampled at the hitpoint.

The `ThinLens2D` class represents the approximation of a thin lens according to [5]. It takes the radius and desired focal length and constructs an object whose only fundamental shape is a `Line2D` shape representing the thin lens. Once a ray hits the line the ray is terminated and a new ray pointing in the direction of refraction is generated at the hitpoint.

Mirror2D Mirrors like lenses are commonly used in optical systems. Most of the time one wants to optimize the shape of a mirror system in order to fulfill some optical property. As all objects in the framework, mirrors are also considered to be rotationally symmetrical. The mirrors implemented in the `Mirror2D` class consist of line segments of the class `Line2D`, the amount of which can be given as an argument to the constructor. Additionally, the shape of the mirror can be given as a parametrized 2D curve. The function should take a single parameter $t \in [0, 1]$ and return 2D points along the curve. The parameters of the shape function can then be changed by the simulation in an optimization algorithm and the mirror reconstructed with the updated values using the *rebuild* method. Naturally the action of the `Mirror2D` object is to reflect the ray according to Eq. (7).

Grid2D The `Grid2D` class offers to simulate quantities distributed within a medium. Rays are traced according to the laws in Eq. (8), Eq. (10) and Eq. (12). When the ray first hits the medium a hit action can be given if the hitpoint contains relevant information to the user. Then the distance within each cell the ray is travelling through is evaluated. It is to be noted that it is assumed the medium is homogenous and has constant refractive index. Thus, the rays travel in a straight line within the medium. Additionally, to the hit action a cell action can be given as a parameter to the constructor. The cell action function is executed once the ray hits a cell. The distance travelled through the cell is evaluated and given to the cell action function, which then in turn can access the cell values in order to change them. The tracing within the grid is done using a fast 2D voxel algorithm shown in [1]. Here the cells are accessed in order the ray traverses them, which is important should the cell action change the ray parameters in any way.

Absorbing media are modelled using the `Grid2D` class and supplying a cell action that evaluates the lost power via Lambert’s law of absorption. It describes the exponential decay of the remaining power of a ray of light in an absorbing medium depending on the coefficient of absorption of the medium and the distance travelled. The remaining power of a ray of light is then given by Eq. (15).

$$P_{rem} = P_{ray} \cdot e^{-\alpha(\lambda)d} \quad (15)$$

Here the absorption coefficient is α and the distance travelled by the ray is d . In general α depends on the vacuum wavelength of the ray λ . For this reason an absorption spectrum of the medium can be supplied and evaluated at each cell. Since the ray’s wavelength stays constant this evaluation can be optimized by evaluating $\alpha(\lambda)$ only once the ray hits the medium and keeping track of this value for successor cells. The absorbed power is then added to the cells value. Thus, after a full simulation of the scene the absorption profile is known. Additionally, the total irradiation is evaluated when the ray hits the medium, if the user requires this information. Supplying the absorption spectrum can be done by using the various utilities the framework provides. These are described in Section 3.4.6.

3.4.4 Scene

The `Scene2D` class represents an entire simulation setup with a collection of initial rays and objects. Objects can be added to the scene via the *add* method. It also provides functionality for generating the initial rays via different light source setups and implements the tracing algorithm. The tracing

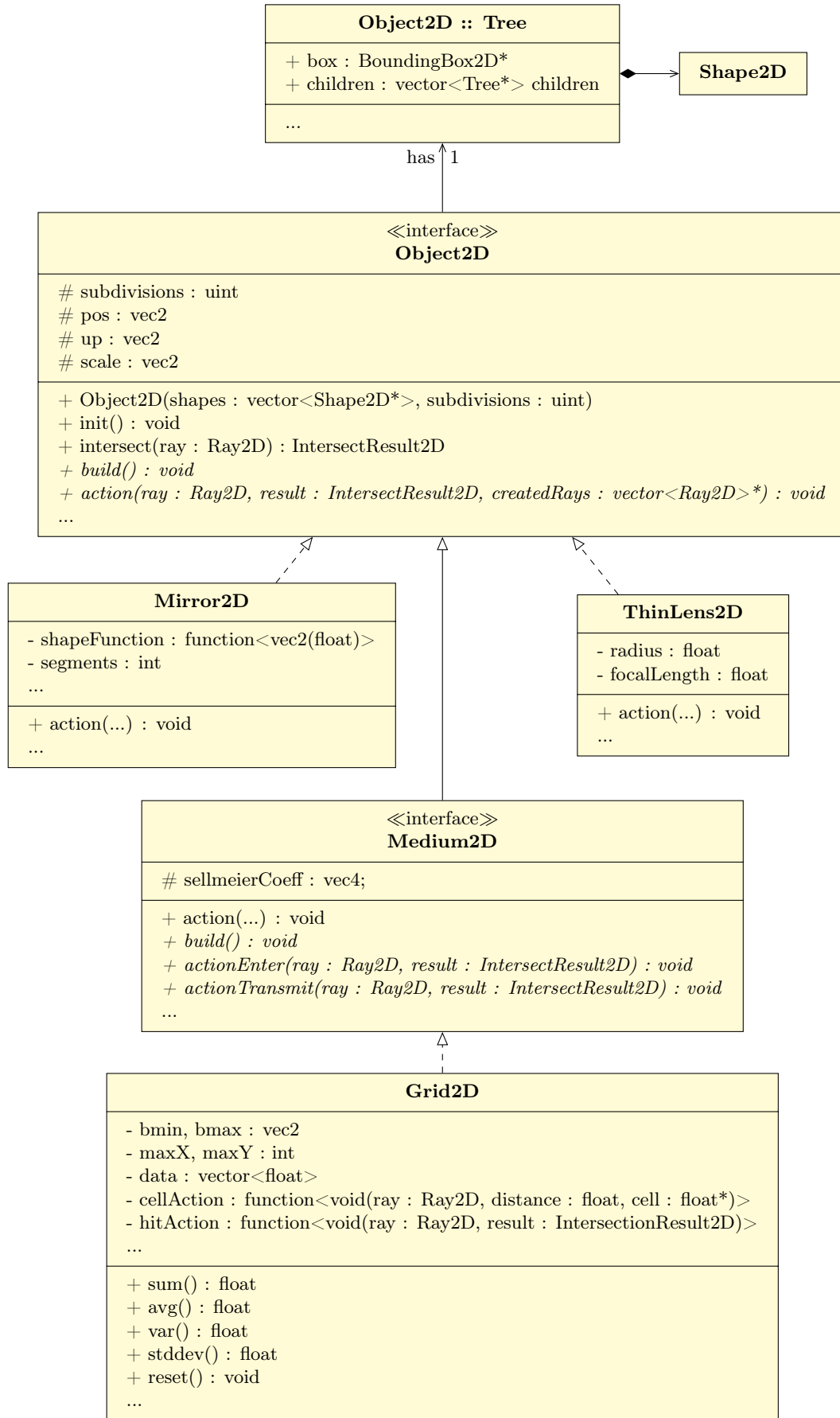


Figure 9: UML class diagram of the Object2D and associated classes

algorithm simulates rays until a certain depth is reached and then outputs all rays that have been created during the simulation. The depth is defined by the number of executed actions by objects along the path of the ray. So suppose two opposing mirrors $mirror_1$ and $mirror_2$ bounce a ray between them. A depth of two is reached once the ray hits the $mirror_1$ object and gets reflected by the objects defined action. The second action is executed by $mirror_2$ when the ray is reflected again on its surface. Because a depth of two has been reached the simulation stops and outputs the created rays for each depth: At depth zero the initially created ray, at depth one the reflected ray which bounced from $mirror_1$ to $mirror_2$ and at depth two the ray which originates at $mirror_2$'s surface and goes to infinity. This way the user can decide which depth is sufficient to simulate the desired phenomena. If one wants to observe the absorption of energy in a thin piece of ionized glass with a weak absorption coefficient it might be required to choose a higher depth in order to bounce the ray through the glass multiple times until the absorbed power becomes insignificant, and a steady state is reached. Theoretically the user can implement a preprocessing step where the simulation is executed multiple times with increasing depth until a steady state is reached, or no more rays are created and choose that depth parameter for the optimization. There are valid reasons though to choose a smaller value than is actually required to reach steady state. If the scene is quite complex and a significant number of rays are needed, it can be necessary to limit the depth in order to reach a result in an acceptable amount of time. The same is true if the absorption for the example above is dominated by the absorption from the first pass of the ray, i.e. the medium has a strong absorption coefficient.

The tracing algorithm starts with the initial rays at depth zero. The rays for the next higher depth are generated by tracing the rays of the next lower depth against the scene. Here rays that have been terminated in the previous depth are ignored and no longer pursued. If a ray has not been terminated it will be tested against all objects in the scene. The intersection results are then stored in an ordered datastructure, sorted in ascending order by the t value of the object intersection result. The actions defined by the intersected objects are then executed in that order. If preceding object terminates the ray or all actions have been executed the iteration is stopped, and the created rays are stored for the current depth. Created rays can also be immediately terminated by the action of the creating object. An example for this would be the refraction of the ray where the transmitted ray is terminated at the boundary of the object and the exiting ray is still traced by the next higher depth. The tracing algorithm of the Scene2D class can be seen in Algorithm 3.

3.4.5 Sampler

The sampling classes implement the sampling techniques discussed in Section 3.3. The abstract interface for sampling is the Sampler class, which is can sample any given datatype. It describes how all other sampling classes are to be used. After construction the sampler needs to be initialized to have an idea about how many samples the user wants in total. Then the user can retrieve samples via the *next* method. The Sampler class also provides an index fields that keeps track of the current index of the sample, should a derived class need that information. One layer below the Sampler interface are interfaces which describe the type of distribution the implemented sampler relies upon. Here the random engines of the STL are usually constructed and initialized with a unique seed. Most specialized sampling techniques for specific datatypes then inherit from those interfaces or use some sort of combination of different random engines. A UML class diagram of the sampler environment is given in Figure 10. Example outputs of predefined sampling techniques are shown in Figure 11.

3.4.6 Utilities

Out of convenience, there are also some utilities included for the user. A VtkWriter class is provided to output the scene, rays and tracing results for included grids. Here the user can specify the percentage of rays to output since it is often not feasible to output all the rays in the simulation but just a representation to observe the behavior of rays. The rays are then sampled uniformly using the Sampler class for each depth. Also, all bounding boxes of objects are output additionally. For the input and output of tables in the CSV format the two CSV classes are provided. The user can

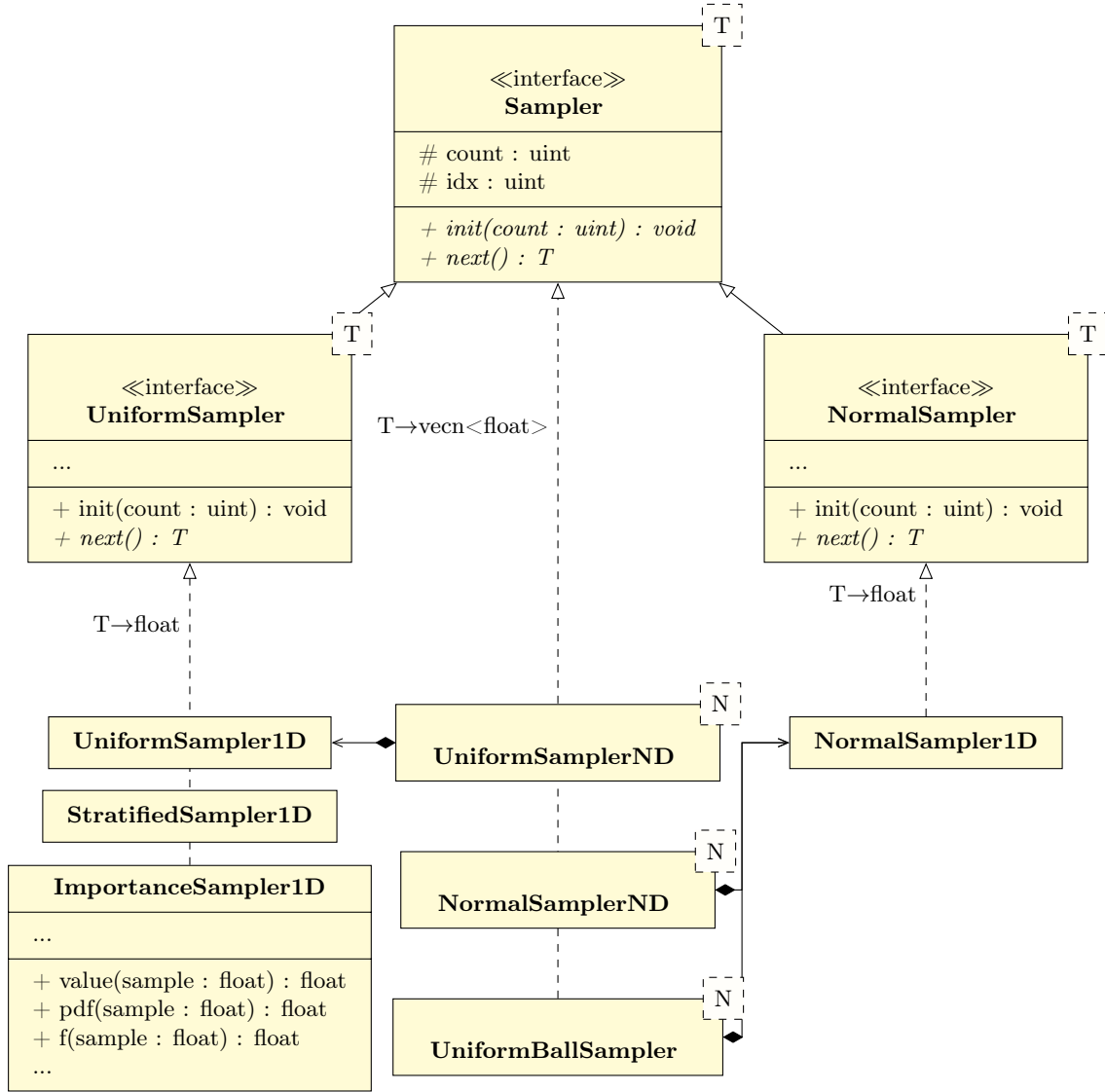


Figure 10: UML class diagram of the Sampler and associated classes

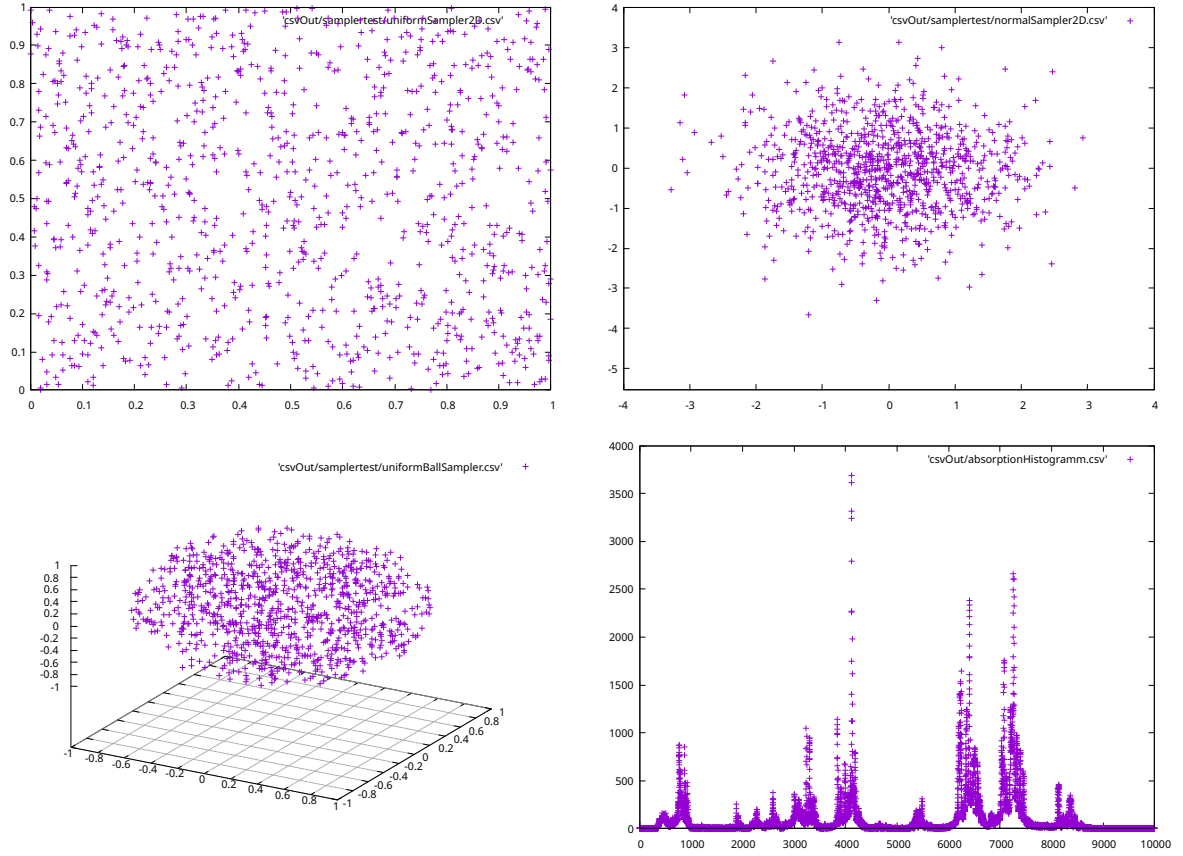


Figure 11: Different examples of sampler output. Two dimensional samplers using the UniformSamplerND (left) and NormalSamplerND (right) classes. A three dimensional uniform ball using the UniformBallSampler class (bottom left) and a histogramm of an importance sampled distribution showing the absorption coefficient for an Nd:YAG crystal (bottom right). Higher value means that the respective index has been sampled more often.

Algorithm 3: Tracing algorithm of the Scene2D class

```
vector<vector<Ray2D>> rays(depth);
rays[0] = startrays;
for  $d$  in 1 ... depth do
    vector<Ray2D> createdRays;
    for ray in rays[d-1] do
        if ray.terminated then
            | continue;
        end
        orderedMap<float, tuple<Object2D*, IntersectResult2D>> intersections;
        for object in objects do
            IntersectResult2D result = object->intersect(ray);
            if result.hit then
                | intersections.insert(result.tEnter, object, result);
            end
        end
        for (t,item) in intersections do
            item.object->action(ray, item.result, createdRays);
            if ray.terminated then
                | break;
            end
        end
    end
    rays[d] = createdRays;
end
```

specify the datatype for each column in the CSV file, so the values are parsed accordingly. Probably the most important part of the included utilities are the function utilities. The collection of methods provide the implementation for lookup functions and other operations done on real valued functions. For example the datapoints from the CSVReader can be sorted and linearly interpolated and the corresponding lookup function returned. The lookup function the uses a binary search algorithm to determine the interpolated value as efficiently as possible. This is particularly important if the user wants to evaluate a function in one of the raytracing action functions. Furthermore, a timer class is implemented to enable accurate timing measurements and an argument parser is provided. As a part of the Maths module commonly used physics laws are implemented such as Snell's law, the Fresnel laws etc.

4 Optimization

4.1 Optimization Methods Overview

In fields like scientific computing and artificial intelligence finding some minimum of a function is a common problem. For a given function $f : \mathbb{R}^n \rightarrow \mathbb{R}$ and a domain Ω the problem is described by Eq. (16).

$$\begin{aligned} \text{Find } \mathbf{x}_{min} \in \Omega \subseteq \mathbb{R}^n \quad \text{s.t.} \\ f(\mathbf{x}_{min}) \leq f(\mathbf{x}) \quad \forall \mathbf{x} \in \Omega \end{aligned} \tag{16}$$

To solve these kinds of problems a multitude of numerical optimization methods are employed. Since the applications of numerical optimization are so diverse in nature, the functions to optimize often have a wide variety of mathematical properties that can be exploited in order to solve the problem more quickly or more accurately. A general rule for choosing an optimization algorithm for a given function, is to use any information available beforehand just by the description of the problem. For example, one might know that the function's second derivative is strictly positive, implying that the shape of the function is convex. With this knowledge one can deduct that there is a global minimum, thus the algorithm can be chosen accordingly, and that the solution of this algorithm will be the global minimum. Unfortunately it is often the case that many properties of a physical simulation can only be evaluated using complex program codes and cannot be described in a linear or even closed mathematical form and thus produce nonlinear dependencies on the input parameters.

To solve these class of nonlinear optimization problems one employs iterative methods that should converge to a solution within a finite amount of steps. The definition of optimality is also of concern when defining what condition actually constitutes a solution. In the most cases one wants to find the global minimum as described in Eq. (16). Knowing that the minimum which is found by any method is actually the global minimum is not possible in general. It can be proven mathematically [18] that it is only possible to know for convex functions, but for non-convex functions a lesser optimality criterium for local minima has to suffice. A modified optimality criterium for non-convex functions is given by Eq. (17) where a local minimum is reached once the function value is smaller than all other function values in an epsilon ball B_ϵ around the minimum.

$$\begin{aligned} \text{Find } \mathbf{x}_{min} \in \Omega \subseteq \mathbb{R}^n \quad \text{s.t.} \\ f(\mathbf{x}_{min}) \leq f(\mathbf{x}) \quad \forall \mathbf{x} \in B_\epsilon(\mathbf{x}_{min}) \end{aligned} \tag{17}$$

Depending on the knowledge about the function f , one has to choose between a large number of iterative methods. Iterative methods can be roughly categorized into second-order, first-order and zero-order optimization algorithms. The second-order algorithms rely on the second derivative or Hessian matrix of the function to converge. First-order methods evaluate the gradient of the function, whereas zero-order methods only need to evaluate the function itself. As stated before, neither of these categories is better or worse per se but depending on the problem at hand some algorithms may perform better than others. "Better" in this context can also mean completely different things depending on the use case. In a microcontroller controlling the flightpath of a rocket time constraints may be significantly more important than scientific calculations running in a laboratory analysis. The main difference of the three types of categories is accuracy and time constraints. The Newton method [18] - a second-order method - chooses the stepsize after evaluating the steepest descent direction optimally using the Hessian matrix, thus needing a fewer amount of steps and delivering an accurate solution to the problem. But on the other hand if one does not have the second derivative in a closed form already, computing the Hessian matrix needs $O(N^2)$ function evaluations, whereas the gradient descent method - a first-order method - only needs to evaluate the gradient, which takes the order of $O(N)$ function evaluations. As a tradeoff the stepsize in the gradient descent method is not known and can be chosen too large, in this case constantly overshooting the solution and never satisfying the stop criterium, or it can be chosen too small, needing a lot of unnecessary iteration steps to finally reach the solution.

Unlike the optimization of well posed analytical problems, scientific simulations are often hard to analyze in terms of slope and curvature, and often produce non-smooth noisy results. Disregarding the noise, some problems might even be smooth and differentiable for a certain neighborhood of values but non-smooth for others. To identify these neighborhoods is in itself a non-trivial problem, that might involve a large amount of computational expense. Especially for codes that rely on some sort of random number generation the goal is often to generate some sampled version of the actual function that is represented at random sample points, so the whole objective is to gradually "uncover" an unknown function where little about the expected result is known beforehand. These types of functions are often called *oracle* functions or *black-box* functions, implying that properties like the slope or curvature are either not well-defined at some points or are not available to the optimization algorithm. This situation can occur in a variety of applications and for a variety of reasons. One reason might be that a small there are some points where the black-box function is non-smooth and therefore not differentiable. So an optimization algorithm that evaluates the gradient directly at those points will deliver incorrect results or will not be stable. Another reason can be that the black-box function might be computationally expensive to evaluate at a single point making the calculation of a gradient or even just part of the gradient infeasible in an iterative context. So the goal in this case would be to optimize a function with a minimal amount of actual function evaluations. For these cases of application zero-order or derivative-free optimization has enjoyed increasing popularity in recent years.

4.2 Derivative-Free Optimization

As discussed in Section 4.1 derivative-free optimization does not rely on the gradient as information for the stepping scheme. This has the advantage that the number of function evaluations is low compared to first-order or second-order methods. Of course this is only the case if the derivatives have to be calculated numerically. If the derivatives are given in a closed form then one generally should use first or second-order methods, as these methods usually exploit this knowledge in some way to get results either faster or more accurately. But if the derivative is not given in a closed form but has to be calculated by evaluating a series of expensive function calls, then derivative-free methods can shine.

As stated by Larson, Menickelly and Wild in [8], "Derivative-free optimization methods are sometimes employed for convenience rather than by necessity". Keeping the strengths and weaknesses of derivative free optimization methods in mind, there always must be a justification to use a certain method. In this work a ray tracing simulation provides a function value (or multiple) depending on some geometric parameters of the simulation setup. There are three major reasons why it was decided to use derivative free approaches to optimize those geometric parameters. The first reason is that there are configurations in the simulation setup where the function value is discontinuous. This can be seen in Figure 12 where a two-dimensional domain was evaluated quite densely to make the discontinuous parts visible. Of course this cannot be done during the optimization algorithm, because it would take a lot of computational cost to just evaluate the whole domain. To sample the function as densely as in Figure 12 in higher dimensions one would have to sample exponentially many more points depending on the dimensions.

Another reason why it was chosen to use derivative free optimization is the computational cost associated with evaluating the function. One evaluation amounts to an entire raytracing simulation of the scene using a significant amount of rays and detail in the scene to achieve low noise. As most derivative free algorithms are specifically designed to minimize the amount of function evaluations, this is the main reason why a black box optimization algorithm was chosen. Especially since the simulation is intended to be used with multiple dimensions of free parameters, each additional dimension would cost a lot in terms of gradient evaluation. Even more so if one calculates the second-order gradient using central differences. The third reason is that derivative free optimization methods can deal well with noisy input. This is particularly useful if the function is evaluated with some sort of random sampling involved. In this work the ray tracer calculates the absorption of light in a transmissible medium. The geometry, power, and wavelength of the rays in the scene are randomly sampled. This means that across multiple evaluations of the function the result varies slightly due to noise generated by the random sampling. This is a common problem in raytracing and can only be reduced by sampling more often, i.e. shooting more rays into the scene. Since

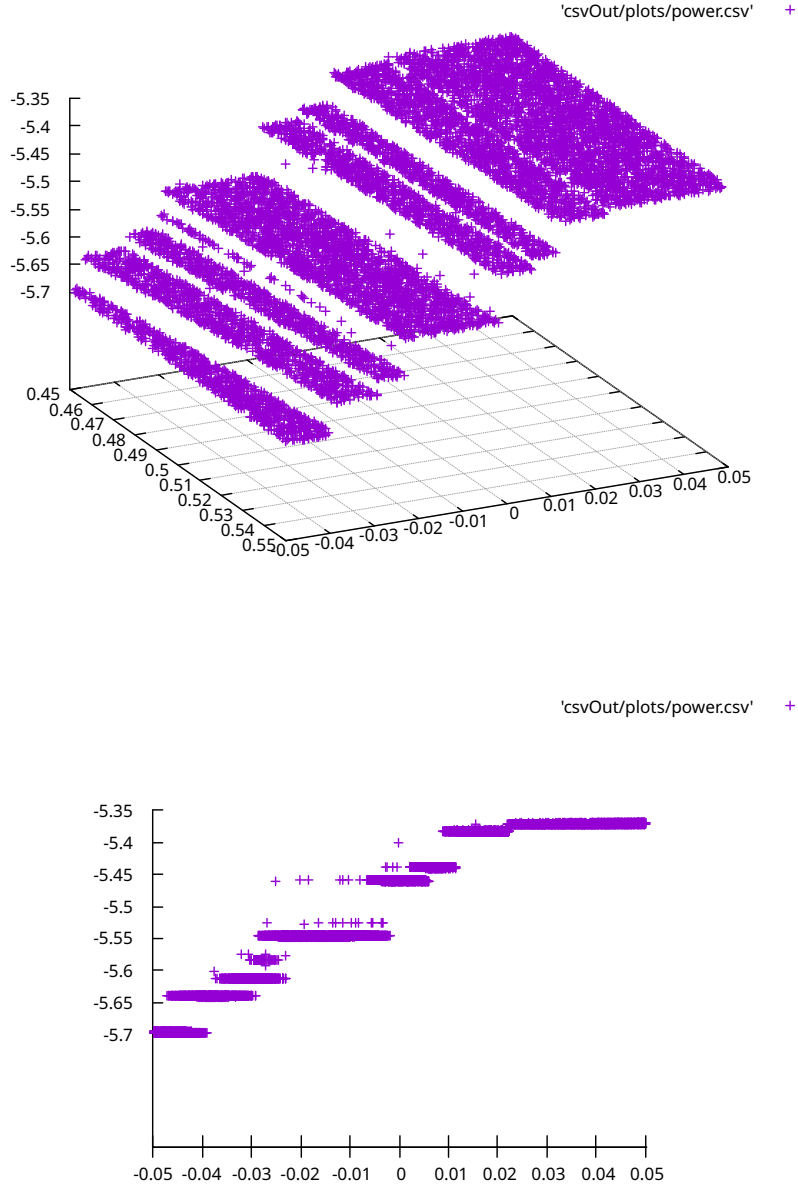


Figure 12: Discontinuous (top) and noisy (bottom) points of an objective function resulting from a ray tracing simulation. The bottom plot is just the same plot as the top one but rotated to make the noisy points more visible. The simulation was carried out using a similar setup to the setup described in Section 5 but with a parabolic mirror of the form $a * x^2 + b$ where a and b are would be the two input parameters to the optimization algorithm. It can be observed that the objective function is more a stepfunction than a continuous one, making the calculation of a gradient using finite differences impractical. Additionally, one can observe that the function has deterministic noise on top of the discontinuity.

the computational cost has to be limited for a function evaluation in some capacity the noise level cannot be reduced to zero completely. It is to be noted though that during the simulation all random variables are kept the same and the sampling only occurs during the setup process of the simulation. Thus, two evaluations of the function with the same parameters deliver the same result. This means that there is noise, but the noise is deterministic in nature. Evaluating a gradient with noisy values is generally a bad idea and will lead to large variance in the direction in the calculated gradient. One could resort to just averaging the gradient across a larger domain of points in order to smoothen the noise. While this is certainly possible it comes with even more computational cost than just calculating the gradient normally. Additionally, there is no easy way to calculate a gradient analytically. It is technically possible to generate an algorithmic differentiation as an alternative to derivative free methods as discussed in [8]. The idea here is to generate a derivative by evaluating the written code and applying the chain rule for differentiation for the elementary operations the code executes. This can work well for simple codes and codes without a significant amount of absolute values and conditional jumps. But after considering that raytracing basically consists of trigonometric functions, absolute values and conditional jumps it was deemed impractical to try an approach with algorithmic differentiation. For these reasons gradient based and therefore also second-order methods along with algorithmic differentiation was not used in this work and derivative free methods were preferred instead.

There are also multiple types and categories of derivative free optimization. These split into two general types. Deterministic methods are methods where the decision process of the algorithm only depends on information gathered and not as in randomized methods also on some factor of randomness introduced by a random variable. These types of optimization then also depend on whether the black-box function is itself deterministic or has stochastic elements to it. As described above, in this work the black-box function is noisy, but the evaluation is strictly deterministic. Therefore, here only methods are explained where the function is deterministic. Perhaps confusingly one can still apply randomized methods on a deterministic function. This can have the benefit of not getting stuck on stationary saddle points as easily as deterministic methods. In fact most presented methods can be extended to use some factor of randomization and thus becoming randomized methods. Also, there are hybrid methods which use some parts of each subtype making the distinction between methods not as clear. As in this work the deterministic MADS algorithm is used on a deterministic but noisy function, only deterministic methods relevant to the understanding of MADS are explained.

The first family of deterministic methods are direct search methods of which the later used MADS [2] algorithm is also a part of. Direct methods do not attempt to approximate some sort of gradient and generally evaluate a selection of points in order to advance towards a minimum. These are split into simplex methods and directional direct search methods.

Simplex methods use a simplex vertex structure and a set of operations on those vertices to iteratively advance the vertices to a local minimum. The most well known of which is the Nelder-Mead method, where the vertex with the biggest function value is continuously reflected through a hyperplane spanned by the other points. The simplex can also be expanded, contracted or shrunk depending on the value of the function at the vertex points. It has been shown that the Nelder-Mead method has some drawbacks and convergence of the method to a stationary point is not always guaranteed [8]. For this reason simplex methods were ruled out for the optimization of the problem presented in this work.

The directional direct search methods always have a current point \mathbf{x}_k and a set of poll points generated by some set of directions $\mathbf{d} \in D_k$ and a current step size α_k [8]. The function is then evaluated at those poll points and the point with the smallest value becomes the new search point \mathbf{x}_{k+1} . If there was no poll point with a smaller value the step size α_k is decreased and a new set of poll points is evaluated. It is to be noted that across multiple iterations the set of directions can change from one iteration to the next. A general algorithm for direct search methods was given in [8] as Algorithm 1 and 2 and an abbreviated version is repeated here for the sake of putting the used MADS algorithm explained in [2] and Section 4.3 in this work into better context.

Note that before evaluating the poll points a search step can be executed, where the function can be sampled at some points in hopes to find a better local minimum. This step is optional and can

Algorithm 4: A general directional direct search algorithm for derivative free optimization taken and abbreviated from [8].

```

Set  $0 < \gamma_{dec} < 1 \leq \gamma_{inc}$ 
Set initial point  $\mathbf{x}_0$ 
for  $k$  in  $0, 1, 2, \dots$  do
    Choose a finite set of search points  $Y_k$ 
    for  $\mathbf{y}$  in  $Y_k$  do
        |  $searchpoints \leftarrow f(\mathbf{y})$ 
    end
    Choose best  $\mathbf{x}_k^p$  from  $searchpoints$ 
    if  $\mathbf{x}_k^p = \mathbf{x}_k$  then
        | for  $\mathbf{d}$  in  $D_k$  do
            | |  $pollpoints \leftarrow f(\mathbf{x} + \alpha_k \mathbf{d})$ 
        | end
        | Choose best  $\mathbf{x}_k^p$  from  $pollpoints$ 
    end
    if  $\mathbf{x}_k^p = \mathbf{x}_k$  then
        |  $\alpha_{k+1} \leftarrow \gamma_{dec} \alpha_k$ 
    end
    else
        |  $\alpha_{k+1} \leftarrow \gamma_{inc} \alpha_k$ 
    end
     $\mathbf{x}_{k+1} \leftarrow \mathbf{x}_k^p$ 
end

```

potentially help improve the performance of the algorithm. The different methods of direct search generate the directions D_k differently. As stated in [8], convergence proofs for directional direct search methods require that the set D_k is a so-called *positive spanning set* for the domain Ω . This means nothing more than that the set of directions form a spanning set for describing any point \mathbf{x} in the domain Ω using only positive factors. Meaning that every \mathbf{x} can be written as a sum of directions \mathbf{d}_i and scale factors $\lambda_i \geq 0$ in Eq. (18).

$$\mathbf{x} = \sum_{i=0}^{|D_k|} \lambda_i \mathbf{d}_i \quad (18)$$

If the set of directions D_k is a subset of some fixed positive spanning set D one calls the derived methods *generalized pattern search* methods or GPS in short. The original proposal for the MADS algorithm [2] used in this work contrasts the way MADS chooses those directions compared GPS methods and highlights the advantage of not being limited to a fixed set D of positive spanning directions, especially when it comes to handling of black-box constraints and convergence analysis. This is explained in more detail in Section 4.3.

Other than direct search methods there are also model based methods. Here the black-box function is modelled by surrogate representing the function. When iterating the function is locally approximated by a function that has some desirable properties for optimization. For example a surrogate function could be a polynomial which is known to be smooth and differentiable. The optimization is then carried out by using information the surrogate function provides. As usually the model is not accurate across the entire domain, but only locally around the current search point. The decision if a step should be taken is also influenced by an estimation of the error the model has at that point. Methods that use this information to make decisions are called derivative-free trust-region methods. Once the model has been formed around the current search point the gradient of the model has to be evaluated. This now is possible in a closed form as the mathematical description and properties of the model function is known. So the main problem with gradient based methods is circumvented by this approach. One drawback is the reliance on the smoothness of the model function. While the model function is smooth the original black-box function can be highly discontinuous. Thus, the model is either not trusted at the discontinuous points or a larger number of points needs to

be evaluated in order to "model" the discontinuity. These methods work well if the model function can closely resemble the original function. This is a problem in the simulation carried out in this work, since the objective function is discontinuous and noisy.

In conclusion, it was determined that derivative free direct search methods offer the most suitable features for the task at hand. In particular one special form of direct search called the mesh adaptive direct search (MADS) offers the capacity to deal with the non smoothness and noisiness of the objective function in this work. Additionally, it can handle constraints on the input parameters even if they are also given in a black-box or oracle form, something that can come in handy in the design process of any optical system. The MADS algorithm can work with a limited amount of black-box evaluations and prohibits the unnecessary evaluation of the objective function at points that do not satisfy constraints. This is beneficial in the design phase of optical systems as often manufacturing limitations need to be considered when optimizing certain parameters. Furthermore, it offers the capability of solving biobjective optimization, which is also required when optimizing both the absorbed power and the variance of the absorption profile. The MADS algorithm is explained and examined in detail in Section 4.3.

4.3 Mesh Adaptive Direct Search (MADS)

The mesh adaptive direct search class of algorithms was originally proposed by Audet and Dennis in 2006 [2]. It was specifically designed to optimize nonlinear, non-smooth constrained functions. The explanations in this chapter are taken from [2] and theoretical mathematical concepts for the purpose of understanding the inner workings of MADS are added where deemed necessary.

4.3.1 Optimality and Clarke's Calculus for non-smooth Optimization

Usually optimality in an optimization problem of the form as in Eq. (17) is defined by the notion of stationary points. A stationary point is a point where the gradient goes to 0 in all directions [18]. Therefore, a stationary point \mathbf{x} must satisfy Eq. (19).

$$\nabla f(\mathbf{x}) = 0 \quad (19)$$

For most cases this criterium is adequate if the function f is differentiable. Since the direct directional search methods were mainly developed to optimize non-smooth functions, one needs a more general way of defining optimality. Defining optimality in a different way implies that a substitute definition of the derivative or differentiability as a whole is required. There are many ways of defining some sort of generalized derivative. One way of defining a generalized gradient is described by Clarke in [6]. Here Clarke proposes a gradient which consists of a set of vectors rather than a single vector. To understand Clarke's definition, a few mathematical definitions and explanations are needed beforehand.

Definition 1 *Let X be a Banach space. A real valued function f is locally Lipschitz continuous in \mathbf{x} if for every $\mathbf{x} \in X$ exists a neighborhood N_x and a Lipschitz constant K_x s.t. for every $\mathbf{y}, \mathbf{z} \in N_x$ holds*

$$|f(\mathbf{y}) - f(\mathbf{z})| < K_x |\mathbf{y} - \mathbf{z}| \quad (20)$$

A function f is called locally Lipschitz continuous if it is locally Lipschitz continuous for every $\mathbf{x} \in X$.

Definition 1 is just a restriction of Lipschitz continuity to a neighborhood around a point. Lipschitz continuity basically says that the function is continuous in that point and the slope of the function is bounded by the constant K_x . Lipschitz continuity in that sense is even stronger than continuity since additionally to normal continuity the slope has to be bounded.

Definition 2 *Let $\{a_n\} \subset \mathbb{R}$.*

$$\lim_{n \rightarrow \infty} \sup a_n = \lim_{n \rightarrow \infty} A_n \quad (21)$$

where

$$A_n = \sup\{a_n, a_{n+1}, \dots\} = \sup\{a_k | k \geq n\} \quad (22)$$

The limit superior of a series a_n is just the limit of a series, which consists of the smallest upper bounds for a modified series, which starts at increasingly later points in the original series. One can think of a value that is the smallest possible value that is an upper bound of a series (function values) at $n \rightarrow \infty$. So basically one is not interested in the bounding values in the start of the series but in the bound which eventually is a bound for all values except for a finite amount of values. With those definitions Clark defined the generalized directional derivative as in Definition 3.

Definition 3 *Let X be Banach, $\mathbf{v} \in X$ some direction and $f : X \rightarrow \mathbb{R}$ a real valued function that is locally Lipschitz continuous. The generalized directional derivative or Clarke directional derivative of f at \mathbf{x} in direction \mathbf{v} is given by*

$$f^\circ(\mathbf{x}; \mathbf{v}) = \lim_{y \rightarrow \mathbf{x}; \lambda \downarrow 0} \sup \frac{f(\mathbf{y} + \lambda \mathbf{v}) - f(\mathbf{y})}{\lambda} \quad (23)$$

The Clarke directional derivative represents an upper bound for the slope in direction \mathbf{v} as one gets closer and closer to \mathbf{x} . This is useful since at some point the slope is definitely bound because of local Lipschitz continuity of f . It guarantees that the Clarke directional derivative always exists for locally Lipschitz continuous functions and the value of f° is a finite quantity [6]. Colloquially one could say that if one knows that the function always has some neighborhood around the current point where the slope is bounded, the slope in a certain direction can be defined as the slope one finds as one takes infinitely many samples of the slope at closer and closer points to the current point, where one wants to find the slope. This slope then is steeper than almost all sampled points - almost all in the mathematical sense means except for a finite amount of points - and it is finite. This circumvents the problem of a derivative defined only with the differential quotient, as those can become infinite or undefined if the function does not behave well at \mathbf{x} . Clark then defines a gradient from the directional derivative as a set of directions ξ , where the projection of ξ onto the direction \mathbf{v} is smaller than the directional derivatives for every direction possible.

Definition 4 *The Clarke generalized gradient of f at \mathbf{x} is*

$$\partial f(\mathbf{x}) = \{\xi \in X : f^\circ(\mathbf{x}; \mathbf{v}) \geq \langle \xi, \mathbf{v} \rangle\} \quad \forall \mathbf{v} \in X \quad (24)$$

This definition of a gradient is not used in the algorithm itself but is helpful to understand why the algorithm converges even for non-smooth functions. It can be proven that for differentiable functions the Clarke generalized gradient collapses to a set with a single element, that being the conventional gradient $\nabla f(\mathbf{x})$ [2]. If function is optimized using GPS methods that produce $\hat{\mathbf{x}}$ as a solution for the minimum, it has been shown by Audet and Dennis as stated in [2] that the conventional gradient is 0 if the function is differentiable in $\hat{\mathbf{x}}$. In particular a stationary point as in Eq. (19) was reached. But for only locally Lipschitz continuous functions it was shown in a convergence analysis by Audet and Dennis that the Clarke generalized directional derivatives are non-negative for the finite set of fixed directions used in GPS methods. If the criterium for optimality is just the statement that the Clarke generalized directional derivatives have to be non-negative along the pattern directions, then GPS methods can provide adequate solutions. But this restriction to the finite set of directions produces a weaker optimality criterium than the one fulfilled by the MADS class of algorithms. The criterium for optimality for MADS methods is thus given by reaching a Clarke stationary point and is defined in Definition 5.

Definition 5 *A point $\hat{\mathbf{x}}$ is called a Clarke stationary point, if the following holds*

$$f^\circ(\hat{\mathbf{x}}; \mathbf{v}) \geq 0 \quad \forall \mathbf{v} \in \mathbb{R}^n \iff 0 \in \partial f(\hat{\mathbf{x}}) \quad (25)$$

This definition also neatly showcases a more intuitive way of thinking about the Clarke generalized gradient. One can think of the set of vectors in the gradient as the directions populating a tangent cone limited by the corresponding Clarke directional derivatives at that point. If the cone has a positive slope on all sides, the point is a minimum. Therefore, the new formulation of the optimization problem for the MADS class of optimization algorithms is just given by finding a Clarke stationary point within the domain Ω . Of course for this to happen one would need to sample infinitely many directions, which is not possible in the optimization algorithm. But as with

optimization strategies using the normal definition of stationary points in Eq. (19) it is enough to come asymptotically close to fulfilling the criterium. Whereas in practice one terminates an iterative algorithm using normal gradients when the length of the gradient is small enough - usually below some threshold ϵ - it can also be said for the MADS class of algorithms that it is enough that the directions are asymptotically densely sampled. Meaning that there is no inherent restriction of which direction can be chosen by the algorithm and enough directions have been sampled to say the criterium has been fulfilled with a certain degree of confidence.

4.3.2 Constrained Optimization with the Barrier Approach

Another advantage that MADS algorithms have is the handling of constraints. For this it is necessary to revisit the definition of the optimization problem once again. Constraints usually have to have a special form for most algorithms. Either they need to be linear, bounded, or differentiable and so on. For the constrained optimization with MADS algorithms none of those properties are required. The constraints can just be given as black-box functions or oracles which decide whether a point satisfies the constraint or not. A big limitation of GPS methods is the directional dependence of evaluating constraint functions caused by the restriction of the poll directions to finitely many fixed directions. In MADS algorithms the black-box constraints c_i are included to arrive at the updated version of the optimization problem in Eq. (26).

$$\begin{aligned}
& \text{Find } \mathbf{x}_{min} \in \Omega \subseteq \mathbb{R}^n \quad \text{s.t.} \\
& f_{\Omega}^{\circ}(\mathbf{x}_{min}; \mathbf{v}) \geq 0 \quad \forall \mathbf{v} \in \mathbb{R}^n \iff 0 \in \partial f_{\Omega}(\mathbf{x}_{min}) \\
& \text{where } \Omega = \{\mathbf{x} | c_i(\mathbf{x}) > 0 \quad \forall c_i\} \\
& \text{and } f_{\Omega}(\mathbf{x}) = \begin{cases} f(\mathbf{x}) & \mathbf{x} \in \Omega \\ \infty & \mathbf{x} \notin \Omega \end{cases}
\end{aligned} \tag{26}$$

The MADS class of algorithms can use a so-called barrier approach where the constraint functions are just treated as points where the objective function goes to infinity. This is possible, because there is asymptotically dense polling of directions, so the barriers are accurately found during the iteration. The optimization is then carried out as if the domain is unconstrained. It is important to note that the barriers $\delta\Omega$ are not evaluated beforehand but are only found during the iteration by sampling the poll directions and finding those points. The points where one or more of the constraints is not satisfied are often called infeasible points. As stated in [2], "a key advantage of the barrier approach is that one can avoid expensive function calls to f whenever a constraint is violated". This translates to only evaluating the poll directions where the poll point is a feasible point. The definition of Clarke's directional derivative can then be modified so that only feasible points are present in the formula. This modification was originated by Jahn and is also shown and referenced in [2]. Since the modification is quite trivial the definition of optimality using this approach does not change much except that the "sampled" points for building the tangent cone have to be feasible points.

4.3.3 Mesh Generation and Execution of MADS algorithms

As stated in Section 4.2, the generalized algorithm for direct directional search optimization is specialized by the concrete implementation in terms of how to choose the set of directions D_k in each iteration k . The same is also true for the MADS algorithm where the special properties for optimality shown in Section 4.3.1 are only arising due to the asymptotically dense evaluation of poll directions. To achieve this dense sampling of directions, MADS algorithms generate two sets of meshes around the current point. It is important to understand that these meshes only exist conceptually and no actual datastructure is needed to store information about the mesh other than some parameters and values kept track of during the actual iteration. One of the meshes is an actual mesh subdividing the domain in a finite amount of n_D directions D . The set D , like in GPS methods is a fixed positive spanning set spanning \mathbb{R}^n as in Eq. (18). The set D can also be viewed as a $n \times n_D$ matrix and thus the mesh is defined by Definition 6.

Definition 6 The mesh M_k at iteration k is defined by

$$M_k = \bigcup_{\mathbf{x} \in S_k} \{\mathbf{x} + \Delta_k^m D \mathbf{z} \mid \mathbf{z} \in \mathbb{N}^{n_D}\} \quad (27)$$

where Δ_m^k is the mesh size parameter and S_k is the set of already visited points.

This definition of a mesh does not differ from GPS methods yet. The distinction comes once the poll directions are chosen from this mesh. If a trial point does not satisfy one of the constraints, the value of the objective function is just set to infinity without calling f in any way. It is stated in [2] that the constraint functions c_i should be ordered according to how expensive the evaluation of a constraint oracle is. It thus is the responsibility of the user that the cheaper constrained should be evaluated first. The objective function f_Ω is then evaluated at the trial points $\mathbf{x} \in \Omega$. Same as in all directional direct search algorithms the user can select a finite set Y_k of search points on the mesh at the start of an iteration. This has the potential benefit of providing flexibility for the user to exploit some problem specific knowledge about the objective function. The way the user chooses those points does not affect the convergence properties of the algorithm since the "lower bound" for convergence is given by the poll step. If a better point is found during the search step this point becomes the new best value, the mesh size parameter Δ_k^m is increased, and the iteration is continued. If the search step does not yield a better solution then the poll step is executed and a better solution is searched with the trial points produced by the poll directions. Should the poll search also fail, and the current solution still be the best solution, the mesh size for the next iteration Δ_{k+1}^m is decreased to produce a finer mesh and the objective function can generally be evaluated closer and closer to the current best point. The exact rule for updating the mesh size parameter shown in [2] and given in Eq. (28), where $\tau > 1$ and $w^- \leq -1$ and $w^+ \geq 0$ are user defined parameters.

$$\Delta_{k+1}^m = \tau^{w_k} \Delta_k^m$$

$$w_k \in \begin{cases} \{0, 1, \dots, w^+\} & \text{if improved point was found} \\ \{w^-, w^- + 1, \dots, -1\} & \text{else} \end{cases} \quad (28)$$

The difference between MADS and GPS methods is how the algorithms choose the trial points in the poll step. For GPS methods the trial points have to lie a fixed distance away from the current point. This distance is Δ_k^m considering the mesh and means that the trial points can only be one "hop" away from the current point. This inherently limits the possible poll directions to the fixed finite set of directions D given in the generation of the mesh. If the selection of trial points is independent of the current mesh size, the possible trial point are limited by a so-called *frame*. The frame is defined by separate poll size parameter Δ_k^p which limits the mesh distance at which trial point can be from the current point. For GPS methods it holds that $\Delta_k^p = \Delta_k^m$. The MADS class of algorithms on the other hand does not impose such a hard restriction on the frame size. Here it must hold that $\Delta_k^p \geq \Delta_k^m$ for all iterations k . The only additional requirement given to the different size parameters is that the mesh size needs to tend towards zero if and only if the poll size also tends to zero with progressive iterations. This ensures that the sampling of directions is asymptotically dense and the modified definition of optimality in Eq. (26) can be satisfied.

The process of generating the MADS frame is described in [2] and yields a positive spanning set of directions D_k which contrary to GPS methods is not a subset of D . The set of poll points P_k is a set of mesh points which are generated using a non-negative integer combination \mathbf{d} of the directions in D and the mesh size parameter Δ_k^m . The distance of the current best point or also called the *frame center* is also bound by a constant times the poll size parameter Δ_k^p . This ensures that the pollpoints in the frame still lie on the mesh but are limited to a certain distance from the frame center. The formal definition of a MADS frame is thus given by Eq. (29).

$$P_k = \{\mathbf{x}_k + \Delta_k^m \mathbf{d} \mid \mathbf{d} \in D\} \subset M_k \quad (29)$$

The distinct advantage of such a frame definition is that during the optimization iteration of the MADS class of algorithms, the mesh size parameter can decrease more rapidly than the frame

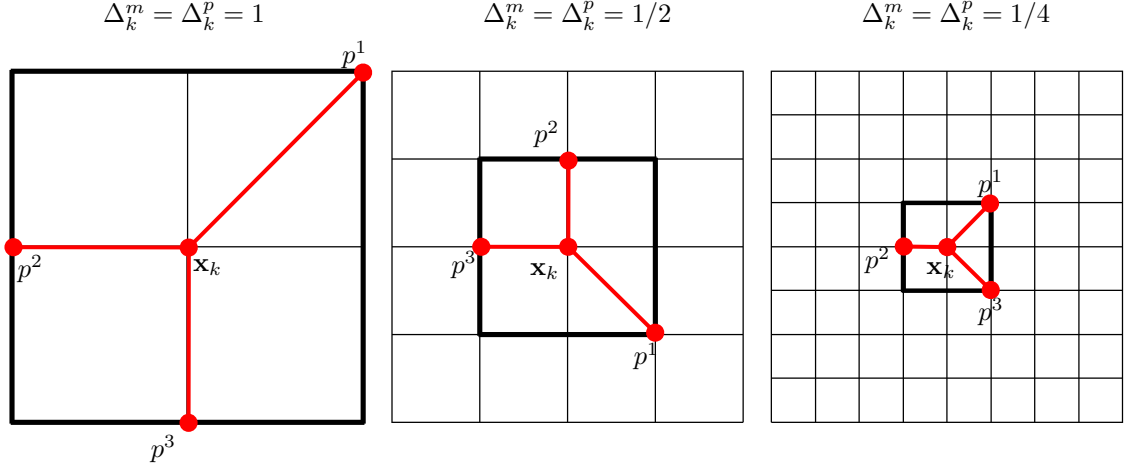


Figure 13: Example of GPS frames $P_k = \{\mathbf{x}_k + \Delta_k^m \mathbf{d} \mid \mathbf{d} \in D_k\} = \{p^1, p^2, p^3\}$ for different values $\Delta_k^m = \Delta_k^p$. Observe that the possible polling directions are limited to the original set D and thus $D_k \subseteq D$. The figure was redrawn from Figure 2.1 in [2]

size parameter. For a GPS method where those two parameters are always equal the number of possibilities for poll directions is finite and fixed. Now suppose that the MADS algorithm iterates indefinitely and always fails to find a better solution point, meaning that the mesh and frame size is successively reduced. It is ensured that if $\Delta_k^p \geq \Delta_k^m$ holds for all iterations, and the mesh size is reduced more rapidly than the poll size, the number of possibilities for the poll directions within the frame tends towards infinity, thus producing a dense set of directions in the limit. Now if all those poll points still do not deliver a better point after a certain threshold of iterations or evaluations one can say that in the limit the condition for optimality using Clarke's generalized gradient is fulfilled. This is indeed proven in [2] and the reader is encouraged to look at the proof themselves as it is enough for this work to understand the inner workings of the MADS algorithm, but keeping the convergence analysis for the reader to discover. A nice visual example of what a MADS iteration looks like compared to GPS iterations is also given in [2] and is also shown here, as the quite theoretical definitions become intuitively clear when one understands the mesh and frame adaptation visually. The example illustrates how a finite set D of mesh directions in \mathbb{R}^2 can generate an infinite amount of poll directions for the MADS algorithm but a finite and fixed amount of directions for GPS methods. So let the set D be the set of eight directions $\{(d_1, d_2)^T \neq (0, 0)^T : d_1, d_2 \in \{-1, 0, 1\}\}$. Note that D is a positive spanning set for \mathbb{R}^2 . There are eight different distinct positive spanning sets consisting of three directions. The number three is chosen arbitrarily here and can also be up to eight directions but at a minimum three directions are required to generate a positive spanning set D_k . This is due to the fact that factors λ_i for a positive spanning set have to be positive as shown in Eq. (18). So in order to reach every point in \mathbb{R}^2 one needs at least two vectors that would be just a spanning set and one additional direction to have some sort of way to reach negative directions. Examples of what a GPS and MADS iteration could look like for a successful iteration, where a point \mathbf{x}_k stays the best solution for multiple iterations, and different mesh and frame parameters are shown in Figure 13 and Figure 14 respectively. As can be seen in Figure 13 the directions for GPS methods are restricted to come from the set D , because the mesh parameter and the frame parameters are the same for each iteration and the only possible trial points lie on the intersection of the edge of the frame with the mesh. The frames in the MADS iteration in Figure 14 shrink at the rate $\Delta_k^p = n\sqrt{\Delta_k^m}$ which is slower than the rate at which the mesh size parameter is reduced. The trial points can then be selected from all the mesh points inside the frame. In the limit $k \rightarrow \infty$ the amount of possible trial points in the frame and therefore directions in D_k also goes to infinity. This achieves the desired effect that the polling directions in the MADS class of algorithms is asymptotically dense and therefore a Clarke stationary point can be identified.

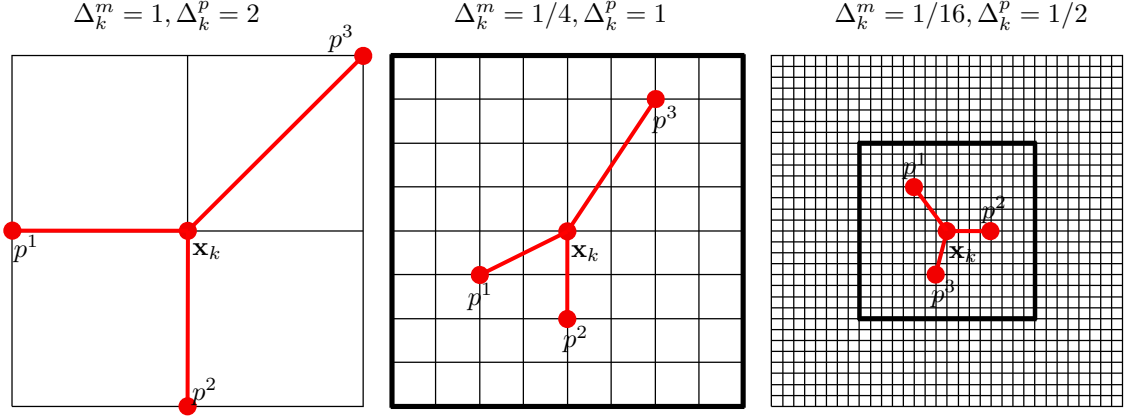


Figure 14: Example of MADS frames $P_k = \{\mathbf{x}_k + \Delta_k^m \mathbf{d} \mid \mathbf{d} \in D_k\} = \{p^1, p^2, p^3\}$ for different values $\Delta_k^m \leq \Delta_k^p$. Observe that the possible polling directions are not limited to the original set D and thus $D_k \not\subseteq D$. The number of possible polling directions goes to infinity and therefore makes the set of sampled directions asymptotically dense. The figure was redrawn from Figure 2.2 in [2]

4.4 Biobjective MADS

4.4.1 Multiobjective Optimization

As discussed in the preceding sections, the problem of single objective non-smooth optimization can be solved using the MADS algorithm. Many optimization problems in scientific computation and engineering applications have to consider multiple objectives at the same time. The optimization problem in this work for example consists of optimizing absorbed power in the laser crystal while at the same time keeping a low variance of absorbed power across the crystal. A high power absorption alone would generate a powerful output beam, but one of low quality, while an even distribution of power alone would create a high quality beam, but the beam would be of low output power. For this reason there is a need to optimize a multiobjective function which describes both power and variance objectives. The multiobjective optimization problem can be formulated as seen in Eq. (30).

$$\begin{aligned}
 &\text{Find } \mathbf{x}_{opt} \in \Omega \subseteq \mathbb{R}^n \quad \text{s.t.} \\
 &\quad F : \mathbb{R}^n \rightarrow \mathbb{R}^p \\
 &\quad F(\mathbf{x}_{opt}) = (f_1(\mathbf{x}_{opt}), f_2(\mathbf{x}_{opt}), \dots, f_p(\mathbf{x}_{opt})) \\
 &\quad \text{is optimal}
 \end{aligned} \tag{30}$$

Note that in Eq. (30) the question of optimality is specifically left vague as in multiobjective optimization a notion of minimum does not make much sense. This is because now the objective function is no longer real valued. It arises the question of what point \mathbf{x} is more optimal than another point \mathbf{y} . One can only somehow compare their vector valued images in F and has to decide what is inherently a better output, a worse output or as a consequence of vector valued outputs an indifferent output. indifferent in this sense means that one cannot say what output is better or worse, but the point \mathbf{x} is better than \mathbf{y} in some objective functions f_i while it is worse in others. This implies there is always a tradeoff in multiobjective optimization and one needs a more fitting definition of what it means for a point to be optimal. A solution to this problem is the definition of *Pareto dominance*, which is explained in [4] and the next chapter Section 4.4.2.

4.4.2 Pareto Dominance and Pareto Fronts

To compare two points in order to determine which point is more optimal than the other, there cannot be a total order relation defined on the image space of F . Instead, there is a partial order relation called *Pareto dominance* relation. As shown in [4], this relation is defined in Definition 7.

Definition 7 Let $\mathbf{u}, \mathbf{v} \in X$ be two points of the multiobjective function $F : X \rightarrow Y$.

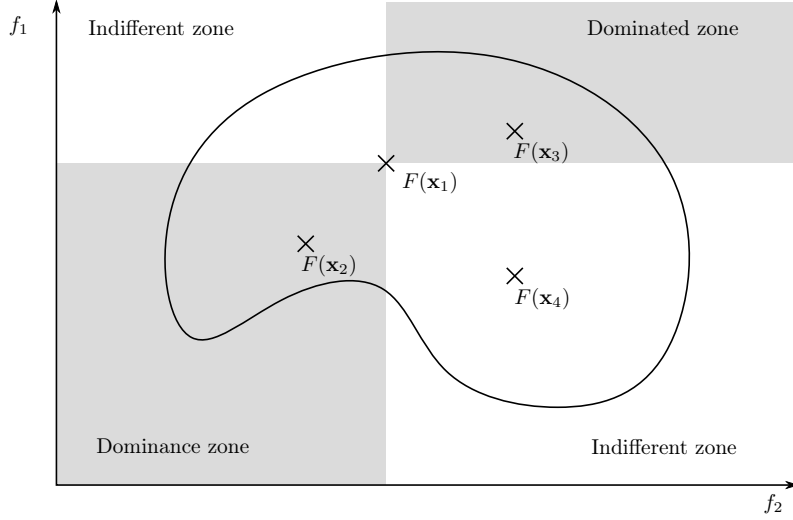


Figure 15: Pareto dominance zones of an image point $F(\mathbf{x}_1) \in Y$. The other points relate to the point \mathbf{x}_1 as follows: $\mathbf{x}_1 \prec \mathbf{x}_3$, $\mathbf{x}_2 \prec \mathbf{x}_1$, $\mathbf{x}_1 \sim \mathbf{x}_4$

- $\mathbf{u} \preceq \mathbf{v}$ (\mathbf{u} weakly dominates \mathbf{v}) $\iff f_i(\mathbf{u}) \leq f_i(\mathbf{v}) \forall i \in \{1, \dots, p\}$
- $\mathbf{u} \prec \mathbf{v}$ (\mathbf{u} dominates \mathbf{v}) $\iff \mathbf{u} \preceq \mathbf{v}$ and $f_j(\mathbf{u}) < f_j(\mathbf{v})$ for at least one $j \in \{1, \dots, p\}$
- $\mathbf{u} \sim \mathbf{v}$ (\mathbf{u} is indifferent to \mathbf{v}) $\iff \mathbf{u}$ does not dominate \mathbf{v} and \mathbf{v} does not dominate \mathbf{u}

For an image point $F(\mathbf{x})$ Definition 7 thus subdivides the image space Y or in this case \mathbb{R}^p into three zones. The first zone is the *dominance zone*, which are all the image points that dominate \mathbf{x} . The *dominated zone* then are all the image points dominated, and the *indifferent zone* are all the image points indifferent to \mathbf{x} . An example of this in \mathbb{R}^2 image space can be seen in figure Figure 15, which is based on Figure 2.1 in [4].

The definition of Pareto dominance alone is not enough to define optimality for multiobjective optimization problems. Like in the single objective case, it is not guaranteed that a problem has a globally optimal solution. For this reason it is necessary to define global and local optimality in terms of the Pareto dominance relation. A definition of global and local optimality for multiobjective problems is given in [4] and here in Definition 8.

Definition 8 Let $\mathbf{x} \in X$ be a point of the multiobjective function $F : X \rightarrow Y$.

- \mathbf{x} is globally Pareto optimal (just called Pareto optimal) \iff There exists no \mathbf{y} s.t. $\mathbf{y} \prec \mathbf{x}$. If \mathbf{x} is Pareto optimal then $F(\mathbf{x})$ is called Pareto efficient.
- \mathbf{x} is locally Pareto optimal \iff There exists an $\epsilon, \sigma > 0$ for which the set $\{\mathbf{y} \in B_\epsilon(\mathbf{x}) \cap X \mid \mathbf{y} \prec \mathbf{x}, F(\mathbf{y}) \in B_\sigma(F(\mathbf{x}))\}$ is empty. If \mathbf{x} is locally Pareto optimal then $F(\mathbf{x})$ is called locally Pareto efficient.

An intuitive understanding of Pareto efficiency is that there cannot be another point in X where all except at least one objective function f_j of the single objective functions f_i are either equal or less than the objective functions at the current point, whereas f_j is truly smaller. As a geometric interpretation in a two-dimensional image space this means there cannot be another point where the image point is to the left or down or both. This is exactly the meaning of dominance zones in Figure 15. An example of Pareto efficient points in \mathbb{R}^2 is given in Figure 16, which is based on Figure 2.2 in [4] with additional explanations. It can be seen that the search for Pareto efficient points returns a set of Pareto optimal points X_p , of which the dominance zone is outside the image space Y . The image Y_p of the set X_p of points is called the *Pareto front*.

The goal of any multiobjective optimization algorithm should be to deliver a set of points which approximates the Pareto front as closely as possible. There are multiple ways of formulating a multiobjective problem as a single objective problem. One way would be to weight the single

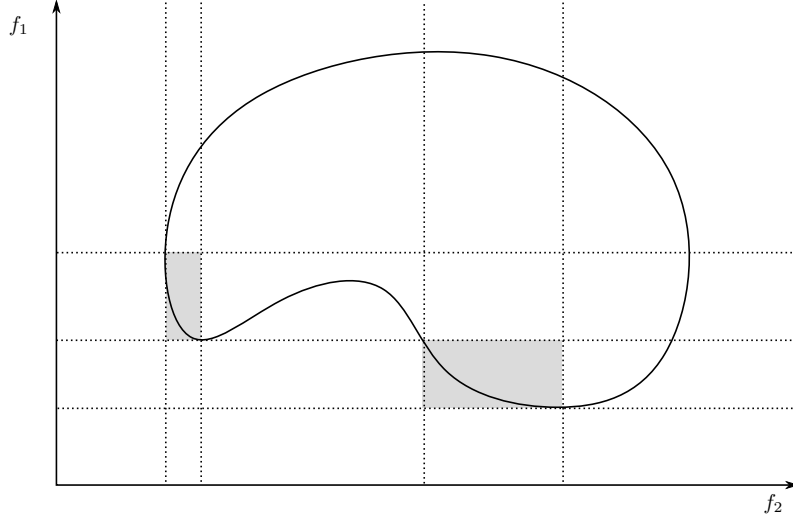


Figure 16: The Pareto front X_p of an image space $Y \in \mathbb{R}^2$ marked with the shaded areas. The condition for a Pareto efficient point is that there is no other point that dominates it. The geometrical interpretation is that there is no point in Y that is to the left or down or both.

objective functions f_i by a factor $w_i \geq 0$ so that $\sum_i w_i = 1$. As stated in [4], any solution to this problem is Pareto optimal for the multiobjective problem. If one solves the linear weighted problem for different combinations, a subset of the Pareto front is generated. The disadvantage of this method is that not all points of the Pareto front can be generated due to the limitation to the linear weighted form. Another method would be to define a reference point $\mathbf{r} \in Y$ and minimizing the q -norm as in Eq. (31), where $1 \leq q \leq \infty$.

$$\min_{\mathbf{x} \in \Omega} \|F(\mathbf{x}) - \mathbf{r}\|_q \quad (31)$$

The reference point approach has the advantage that it can theoretically reach the entire Pareto front. Therefore, solving the reference point problem for different reference point produces an approximation of the Pareto front [4]. The only disadvantage is that if the point is chosen incorrectly also non-efficient points are generated. The general question with the reference point approach is how to choose those reference points. Along with other approaches of solving the multiobjective optimization problem, it is also shown in [4] that a general parametrized approach with respect to the reference point has some properties necessary for optimality in Clarke's calculus, if the parametrization conserves Lipschitz continuity and other properties. The parametrized version of the single objective formulation of a multiobjective optimization problem uses the parametrized function Φ_r as a real valued objective and is shown in Eq. (32).

$$\min_{\mathbf{x} \in \Omega} \Psi_r(\mathbf{x}) \quad \Psi_r(\mathbf{x}) = \Phi_r(f_1(\mathbf{x}), f_2(\mathbf{x}), \dots, f_p(\mathbf{x})) \quad (32)$$

Depending on the choice of Φ_r the Pareto front is approximated if one solves this problem for a set of reference points. This is proven for a bunch of choices for Φ_r in [4] and the reader is encouraged to convince themselves of this property. In the next section the concrete implementation of the BiMADS algorithm for the solution of biobjective non-smooth optimization problems is shortly presented.

4.4.3 BiMADS

The BiMADS algorithm was originally presented by Audet, Savard and Zghal in [4] in 2008. It uses the MADS algorithm to solve a series of single objective formulations of a biobjective problem with increasingly stringent stopping criteria. The idea is to iteratively build a set of non-dominated points that approximate the Pareto front. The set of non-dominated dominated points $X_{\mathcal{L}}$ is updated each

time the MADS algorithm runs and keeping all visited trial points that are non-dominated by the current set $X_{\mathcal{L}}$ and throwing away all dominated points in $X_{\mathcal{L}}$. The single objective problem the MADS has to solve each iteration is a single objective formulation using the parametrized approach in Eq. (32). The reference point is chosen beforehand using a process which is later described in more detail. After the update of $X_{\mathcal{L}}$ the list is ordered in ascending order according to the value of f_1 and in descending order according to f_2 . This is only possible because the amount of objectives is two. The ordering is done in order to easily determine the euclidian distance between the images $Y_{\mathcal{L}}$ of $X_{\mathcal{L}}$. This is done so the point where the euclidian distance in image space Y is the largest to its neighboring points \mathbf{x}_j - note that neighboring here only makes sense because of the ordering of set $X_{\mathcal{L}}$ according to the previous discussed relation defined for only two objectives f_1, f_2 - can be determined and the values of the objectives of those neighboring points can be combined to get a new reference point \mathbf{r} that surely dominates the chosen point \mathbf{x}_j . In short, that BiMADS algorithm choses its' reference points in a way to minimize the gaps between the Pareto efficient points in $Y_{\mathcal{L}}$. This achieves better coverage of the Pareto front. The MADS algorithm is then executed for the single objective problem with respect to \mathbf{r} and started from the chosen point \mathbf{x}_j . Additionally, to choosing the reference point, the algorithm then stores a weighting factor for that specific \mathbf{x}_j in order to achieve better coverage and increase the stopping criterium for MADS should that point be chosen again. Once a reference point \mathbf{r} was derived from a point \mathbf{x}_j the weighting is increased, which then in turn diminishes that points ability to be chosen again in the succeeding iterations. This approach of choosing the reference points gives an even distribution of non-dominated points along the Pareto front. Since the basic idea of the BiMADS algorithm was explained and is sufficient to understand the application of the algorithm in this work, the convergence analysis for BiMADS is left to the reader to study in [4]. A detailed overview of the BiMADS algorithm is given in Algorithm 5.

Algorithm 5: BiMADS algorithm

Initial MADS run to solve $\min_{\mathbf{x} \in \Omega} f_1(\mathbf{x})$ and $\min_{\mathbf{x} \in \Omega} f_2(\mathbf{x})$ at starting point \mathbf{x}_0
Set $X_{\mathcal{L}} = \mathbf{x}_1, \mathbf{x}_2, \dots, \mathbf{x}_J$ to be an ordered list of non-dominated points s.t.
 $f_1(\mathbf{x}_1) < \dots < f_1(\mathbf{x}_J)$ and $f_2(\mathbf{x}_1) > \dots > f_2(\mathbf{x}_J)$
while $\delta_{\hat{j}} > \text{threshold}$ *OR* *maximum iterations not reached* **do**
 if $J > 2$ **then**
 $\hat{j} \leftarrow \operatorname{argmax}_{j=2, \dots, J-1} \delta_j = \frac{\|F(\mathbf{x}_j) - F(\mathbf{x}_{j-1})\|^2 + \|F(\mathbf{x}_j) - F(\mathbf{x}_{j+1})\|^2}{w(\mathbf{x}_j) + 1}$
 Define reference point $\mathbf{r} \leftarrow (f_1(\mathbf{x}_{\hat{j}+1}), f_2(\mathbf{x}_{\hat{j}-1}))$
 end
 if $J = 2$ **then**
 $\mathbf{x}_{\hat{j}} \leftarrow \mathbf{x}_2$
 $\delta_{\hat{j}} \leftarrow \frac{\|F(\mathbf{x}_2) - F(\mathbf{x}_1)\|^2}{w(\mathbf{x}_2) + 1}$
 Define reference point $\mathbf{r} \leftarrow (f_1(\mathbf{x}_2), f_2(\mathbf{x}_1))$
 end
 if $J = 1$ **then**
 $\mathbf{x}_{\hat{j}} \leftarrow \mathbf{x}_1$
 $\delta_{\hat{j}} \leftarrow \frac{\delta}{w(\mathbf{x}_{\hat{j}}) + 1}$
 Execute MADS from $\mathbf{x}_{\hat{j}}$ to solve $\min_{x \in \Omega} f_1(\mathbf{x})$ and $\min_{x \in \Omega} f_2(\mathbf{x})$. Terminate MADS
 when mesh size Δ^m drops below $O(\delta_{\hat{j}})$. *Goto* update step.
 end
 Execute MADS for the single objective formulation Φ_r . Terminate MADS when mesh size
 Δ^m drops below $O(\delta_{\hat{j}})$ or a maximum number of objective evaluations is reached.
 Update $X_{\mathcal{L}}$ by adding all dominant points from the MADS run and removing all
 dominated points. Increase weights $w(\mathbf{x}_{\hat{j}}) \leftarrow w(\mathbf{x}_{\hat{j}}) + 1 \quad \forall \mathbf{x} \in X_{\mathcal{L}}$
end

4.5 NOMAD Library

The MADS algorithm as well as the BiMADS algorithm are implemented in the open source library NOMAD [9]. It was developed by Charles Audet, Sebastien Le Digabel and Christophe Tribes. The library offers a C++ interface to describe black-box optimization problems and solve them using the MADS algorithm. Additionally to the library interface, one can also optimize any user created program in batch mode, which takes inputs and generates outputs in a standardized way. While this approach can help to get a working optimization off the ground quickly, it was decided that the added flexibility and performance of the customizable library interface is better suited for the black-box problem in this work. It is to be noted that the NOMAD library currently is undergoing a rewrite in version 4 and unfortunately some features of version 3 including the BiMADS implementation were missing when trying out the newest version. Thus, the older version 3 of NOMAD available at [3] had to be used in this work.

The integration into the raytracing framework is done by defining a user defined evaluator class inheriting from a NOMAD provided multi objective evaluator. The user then needs to override an evaluation function where the parameter list contains the current point \mathbf{x} . For BiMADS the two objective functions need to be set as an output additionally to the list of constraint functions c_i . Hereby the constraints are of the form $c_i \leq 0$, meaning that if a point dissatisfies a condition a positive value needs to be returned. There are also multiple parameters that need to be set in order to define the optimization problem. The dimension of the problem needs to be defined and the maximum number of black-box evaluations per MADS run needs to be defined. For the constraint functions different types of handling are available. The barrier approach can be set to be enforced rigorously by prohibiting the MADS frame to evaluate infeasible points. There are also more relaxed types of constraint handling, e.g. by allowing infeasible points during the iteration but not as the final solution for a Pareto efficient point. This approach was also chosen in this work as the algorithm can then pass through barriers potentially reaching a better solution on the other side. Also, the type of allowed mesh directions and the number of generated poll points per iteration can be set by a parameter. Unfortunately in version 3 of NOMAD the output of the Pareto front is only available via reading the console output of the BiMADS run or by setting a file as a statistics file. Therefore, if the solutions are required by the user in the parts of the program after the BiMADS run, the user either has to read in the file or reroute the console output and parse the resulting text. NOMAD can also be set to run in parallel based on OpenMP directives by setting the corresponding parameters. In this work the parallelization was not used, but it would be possible to set up an array of scenes each with their own instantiation of the objects in the scene. A list of the available parameters and other instructions for the usage of NOMAD can be found on the website [3] as a user guide for NOMAD 3.

5 Optimization of Pump Light Absorption in a Nd:YAG Solar Laser

In this chapter a conceptual example of a solar pumped Nd:YAG laser is simulated using the ray-tracer framework presented in Section 3 and the BiMADS algorithm presented in Section 4. The BiMADS algorithm is employed to optimize geometric parameters such as mirror shape and positions of optical components. The BiMADS algorithm has two objective functions. One function evaluates the total absorbed power and the other one evaluates the variance of power across the Nd:YAG crystal. To analyze the effect of a high power and low variance absorption in the laser rod, the commercial software ASLD (Advanced Software for Laser Design) [17] was used. ASLD provides thermal and structural analysis of laser crystals employing the finite element method as well as calculation of laser output power and beam quality of a resonator setup using dynamic multimode analysis. The stability of the resonator and the resulting beam radius can also be analyzed. Additionally, ASLD also has an internal 3D raytracer for the analysis of pump light absorption. This is where the obtained mirror shapes and geometrical parameters from the optimization can be loaded into and the resulting output beam is calculated. Different outputs of optimizations with different parameter constraints are presented and discussed.

5.1 Setup and Simulation Parameters

The simulated setup consists of a large Fresnel lens with a diameter of 1.2 m collecting the sunlight and focussing it with a focal length of 1.2 m. The light then hits a reflective mirror bouncing the light onto an Nd:YAG laser rod with a diameter of 6 mm and a length of 95 mm. The free space between the objects is always assumed to be vacuum and therefore has a refractive index of 1 and no light is lost when a ray transverses the free space.

Sunlight is generated in a 1.2 m wide round surface consisting of rays according to the solar spectrum. Hereby the solar spectrum has been importance sampled with respect to the absorption spectrum of an 1% doped Nd:YAG crystal. This is done so the majority of rays in the raytracer actually have a contribution to the absorbed power in the crystal. The rays are also given a divergence equal to the value of solar divergence of 0.53338° . The Fresnel lens is approximated via the thin lens approach described in Section 3.4.3. For now, no assumption for dispersive effects are made for the Fresnel lens. The mirror shape is described using a Bezier curve with 4 control points as in Eq. (33).

$$\begin{aligned} s &: [0, 1] \rightarrow \mathbb{R}^2 \\ s(t) &= \text{Bezier}(t, \mathbf{p}_1, \mathbf{p}_2, \mathbf{p}_3, \mathbf{p}_4) \end{aligned} \tag{33}$$

Hereby the mirror shape is restricted to a monotonous shape along the rotational axis of the setup. This is implemented using a constraint function which compares the control points of the Bezier curve and outputs a value according to the convention for the optimization algorithm as described in Section 4.3.2. Generated line segments are then subdivided using a quadtree as described in Section 3.2. During the optimization the number of line segments is set to 100 per side of the laser rod (upper and lower). The positions of the control points are also input parameters for the optimization step. The Nd:YAG laser rod is a grid with 158 by 10 cells. For dispersion effects within the crystal the Sellmeier coefficients for a Nd:YAG crystal were taken from [22]. Absorption of light within the crystal is modelled using the Lambert law of absorption described in Eq. (15). Hereby the absorption spectrum of a 1% doped Nd:YAG laser rod was used in both ASLD and the optimization program. Additionally, the irradiated power reaching the crystal is tracked when a ray hits the crystal. The distance of the laser rod and the mirror to the Fresnel lens can be opened as a parameter for the optimization. An example setup can be seen in Figure 5.1.

The optimization is done by first executing a random search for maximal absorbed power across all opened parameters which satisfy given constraints to gain an estimate for a good starting point for the constrained BiMADS algorithm. It was observed that if the random search algorithm finds a point that does not satisfy all constraints, the initial MADS runs cannot adequately find Pareto efficient points. This happens even if a soft barrier approach is used. Note that optimal

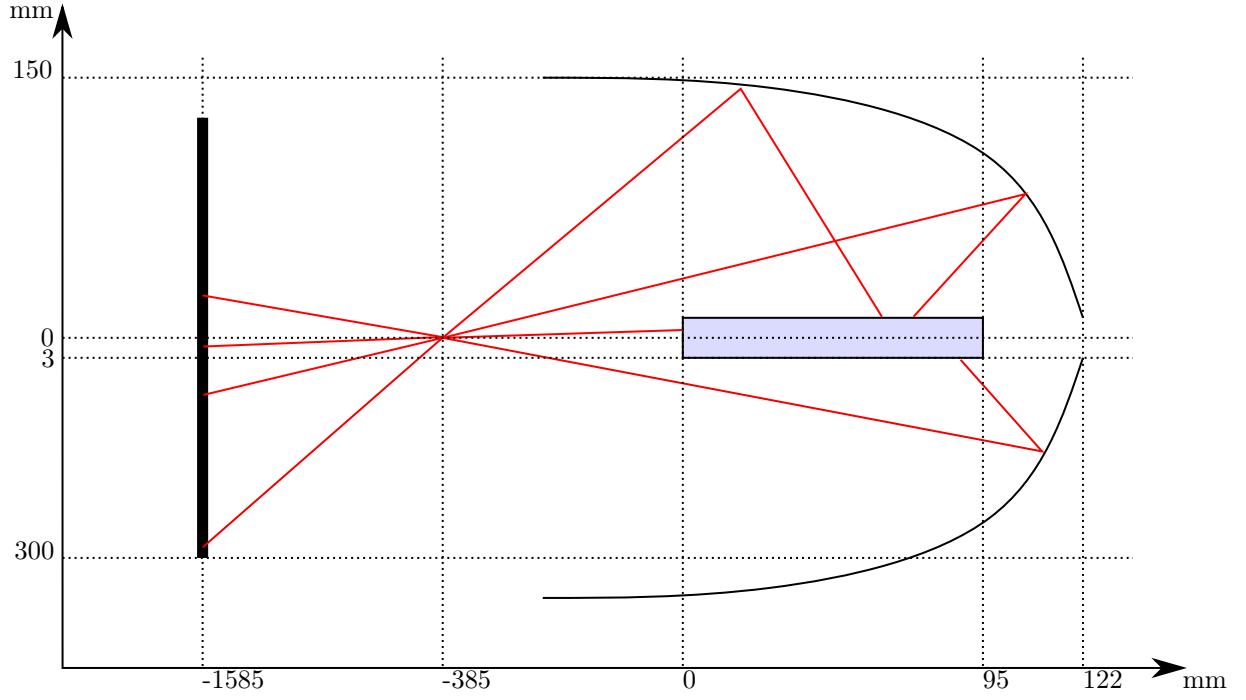


Figure 17: Example setup of the solar laser. The mirror shape is determined using the four control points $\mathbf{p}_1, \mathbf{p}_2, \mathbf{p}_3, \mathbf{p}_4$. The distance from the left side of the crystal to the origin is controlled by the parameter d . When translating the crystal with d the mirror is also translated. Since in the open setups the start and endpoint of the mirror are also open, the position of the mirror relative to the crystal can be controlled via the controlpoints.

here in the random search step means only for one and not Pareto optimal for the two objective functions. Therefore, the random search should either use a method that only generates searchpoints that satisfy the constraints or use the rejection method to reject samples that violate one of the constraints. Since in this case only a single monotony constraint was used, it is easy to generate only samples satisfying this constraint, and it was decided to use this approach. Additionally, it should also be short and used to gain a rough estimate of a good starting point for the objective function for the initial MADS runs for BiMADS.

The two objective functions for the BiMADS algorithm are chosen to be the negated sum of all power values of the cells within the crystal grid and the variance of the cell values. The output of the BiMADS algorithm is an approximation of the Pareto front and chosen points are then traced with a higher resolution of 10000 line segments. The scene is output in the VTK format and the mirror shape is additionally output in a format to be read by ASLD for the beam analysis.

Different outputs of the optimization step for different combinations of allowed values and constraints are presented and observed behavior of the optimization discussed. The main focus is the total amount of absorbed power, in comparison to the input power, which was set at 720 W for the sunlight hitting the Fresnel lens. Furthermore, the variance of absorbed power in the crystal is evaluated for the different constraints. The amount of power hitting the crystal in relation to the pump power can be defined as the irradiation efficiency E_{irr} as in Eq. (34).

$$E_{irr} = \frac{P_{irr}}{P_{pump}} \quad (34)$$

Note that this value is purely the power the crystal is exposed to on its surface. As in a sidepump setup the rays are not only absorbed once but it is possible for rays to hit the medium multiple times, E_{irr} can take on values greater than 1. In fact as can be seen in the sections below, this effect

should be exploited by a good setup. The absorbed power can also be described by defining the geometric optical efficiency as in Eq. (35), where P_{abs} is the amount of absorbed power and P_{pump} is the power of the pump light or in this case the amount of solar power irradiating the Fresnel lens.

$$E_{geom} = \frac{P_{abs}}{P_{pump}} \quad (35)$$

Additionally, one can define an absorption efficiency, which describes the amount of power absorbed in relation to the amount of power hitting the laser rod. This can be seen in Eq. (36).

$$E_{abs} = \frac{P_{abs}}{P_{irr}} \quad (36)$$

Lastly, the total optical-to-optical efficiency is defined as the output power of the laser beam in relation to the pump power. The optical-to-optical efficiency is defined in Eq. (37).

$$E_{opt} = \frac{P_{out}}{P_{pump}} \quad (37)$$

The solutions are compared using these defined efficiencies and the variance of the absorbed power across the crystal. Finally, the solutions for the different runs are compared to each other and a reference solution on the basis of the ASLD beam parameters for continuous wave power output and beam quality. For each solution the setup parameters are presented in a table once again and the VTK output is shown and discussed.

Before presenting the solutions, it is also important to quickly go over the relevant settings used in ASLD, as the optimization program should emulate these parameters as closely as possible or ideally be identical. Hereby only the non-trivial settings specific to ASLD are explained as e.g. the pump power was already explained before and is a trivial setting. The crystal is traced using Snell's law at the sides and using closed faces at the circular faces of the rod. This is done because usually one wants to have some sort of resonator setup around the circular faces of the crystal consisting of two mirrors where no light is able to pass from the outside. Therefore, no power should be transmitted through those faces and a good solution should minimize the loss at the faces. Unfortunately ASLD cannot model the Fresnel laws when refracting rays into the crystal and instead uses a flat transmissibility parameter for all rays independent of the incident angle. This was set to 100% and the optimization program was adjusted to also use this flat transmissibility when refracting a ray. The problem with this approach was observed during optimization and is also shown later when the setups and solutions are explained. The crystals dispersive properties are set to use the Sellmeier coefficients from [22]. The resonator setup consists of two flat mirrors one to the left of the laser rod with a distance of 550 mm and one to the right of the laser rod also with a distance of 550 mm. Here the left mirror has a reflectivity of 100% whereas the right mirror has a reflectivity of 96%.

The reference solution achieved a continuous wave output of 30.52 W, which corresponds to a optical-to-optical efficiency of 4.24% with a beam quality of 4.82 and 4.30 in the x and y direction respectively. It was achieved by the method of feedback compensation of an initial algebraically derived solution, where the intensity of pumplight on the surface of the crystal was meant to be distributed evenly. As one can see later on, this approach disregards many optical effects actually present in a real setup. These effects can make a significant difference in the output power and the beam quality and can only be properly modelled using raytracing techniques. The results in the setups below are chosen to illustrate the most important effects for a solar laser.

5.2 Setup 1: Fixed Crystal Position and fixed Mirror Endpoints

The first setup is based on the constraints given by the reference solution. Mainly the start and endpoint of the mirror is fixed and only the shape in between is optimized. This means that the control points at both ends of the Bezier curve are fixed in place and the problem becomes a 4

| | | |
|-------------------------|---|---------------------|
| Raytracing Settings | Optimization rays | 10000 |
| | Optimization segments | 100 |
| | Final step rays | 100000 |
| | Final step segments | 10000 |
| Optimization Settings | Maximum initial random search black-box evaluations | 10000 |
| | BiMADS Maximum black-box evaluations per MADS run | 1000 |
| | BiMADS constraint type | Progressive barrier |
| | BiMADS poll direction type | Orthogonal N+1 |
| Optimization Parameters | $\mathbf{p}_1.x$ | $4.2mm$ |
| | $\mathbf{p}_2.x$ | $[4.2mm, 75mm]$ |
| | $\mathbf{p}_3.x$ | $[75mm, 150mm]$ |
| | $\mathbf{p}_4.x$ | $150mm$ |
| | $\mathbf{p}_1.y$ | $0mm$ |
| | $\mathbf{p}_2.y$ | $[0mm, 300mm]$ |
| | $\mathbf{p}_3.y$ | $[0mm, 300mm]$ |
| | $\mathbf{p}_4.y$ | $224mm$ |
| | d | $0mm$ |

Table 1: Parameters for Setup 1

dimensional problem, meaning that both control points in the middle have two coordinates that the algorithm can vary. Furthermore, it is not permitted to move the crystal and the mirror assembly in any way. This is done so the results are comparable to the reference solution in a more direct way. The parameter ranges and other optimization related parameters can be seen in Table 5.2.

The optimization was started by an initial random search with a maximum number of black-box evaluations. The resulting startpoint for the BiMADS algorithm and the subsequent best solution can be seen in Figure 5.2. The best solution was chosen from a number of pareto efficient points returned by the BiMADS run. It can be seen that in this case the initial random search solution was already quite close to the best solution returned by BiMADS. The specific values can be seen in Table 5.2. The best solution was solution 1 with a continuous wave output of 35.14 W, which would be an optical-to-optical efficiency of 4.88%. This would be an improvement of 15.14% in terms of power compared to the reference solution. The beam quality also improved in both x and y direction. In Figure 5.2 it can be seen that the solution tries to avoid hitting the circular faces of the rod as much as possible. Furthermore, it can be observed that only a small part of the secondary rays is actually directed towards the crystal. This is likely the biggest loss of power in the pump setup and one of the effects the reference solution disregarded. For this reason it was tried to open up more parameters to the optimization algorithm in Setup 2. The resulting beam widths for Setup 1 in the resonator are shown in Figure 5.2.

| Solution | 1 | 2 | 3 | 4 | 5 | 6 | 7 | 8 |
|----------------------------|--------|--------|--------|--------|--------|--------|--------|-------|
| Absorbed Power[W] | 155.46 | 154.82 | 141.87 | 112.07 | 109.66 | 101.87 | 100.08 | 87.10 |
| Variance[W] | 13.49 | 12.66 | 2.43 | 0.44 | 0.12 | 0.09 | 0.09 | 0.08 |
| Irradiation Efficiency [%] | 130.78 | 130.02 | 116.74 | 85.98 | 84.19 | 78.73 | 77.33 | 67.15 |
| Optical Efficiency [%] | 21.59 | 21.50 | 19.70 | 15.57 | 15.23 | 14.15 | 13.90 | 12.10 |
| Absorption Efficiency [%] | 16.51 | 16.54 | 16.88 | 18.10 | 18.09 | 17.97 | 17.98 | 18.01 |
| cw Output@720W [W] | 35.14 | 35.04 | 25.91 | 17.00 | 16.43 | 14.57 | 13.45 | 8.56 |
| Beam quality x | 4.25 | 3.66 | 4.81 | 4.07 | 4.25 | 3.88 | 3.72 | 3.00 |
| Beam quality y | 3.22 | 3.11 | 4.32 | 4.07 | 3.49 | 3.71 | 3.52 | 2.87 |
| $\mathbf{p}_3.x$ [mm] | 71.76 | 71.38 | 75.00 | 58.86 | 58.12 | 55.30 | 55.00 | 0.89 |
| $\mathbf{p}_4.x$ [mm] | 127.66 | 127.86 | 129.66 | 119.63 | 120.01 | 117.17 | 116.90 | 78.08 |
| $\mathbf{p}_3.y$ [mm] | 0.01 | 0.02 | 0.53 | 14.05 | 13.73 | 14.94 | 14.75 | 3.22 |
| $\mathbf{p}_4.y$ [mm] | 136.47 | 134.67 | 128.55 | 105.85 | 109.47 | 106.74 | 107.39 | 17.17 |

Table 2: Pareto optimal points for Setup 1 with initial random search

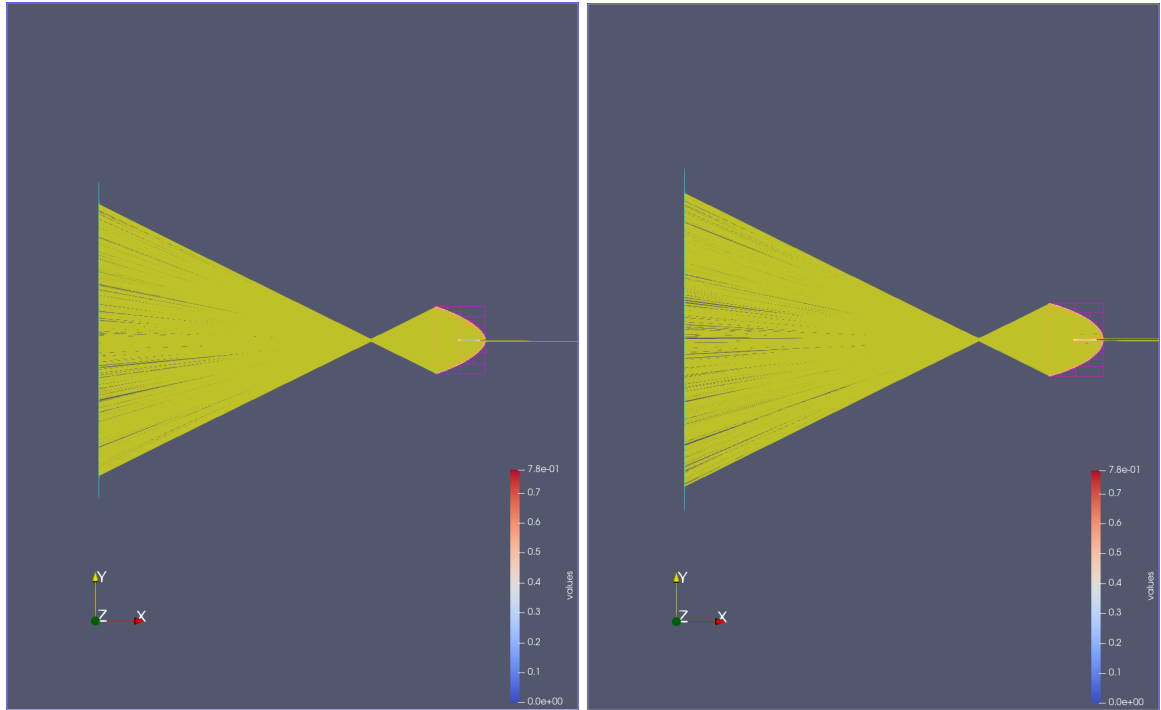


Figure 18: VTK Output for Setup 1 with initial random search

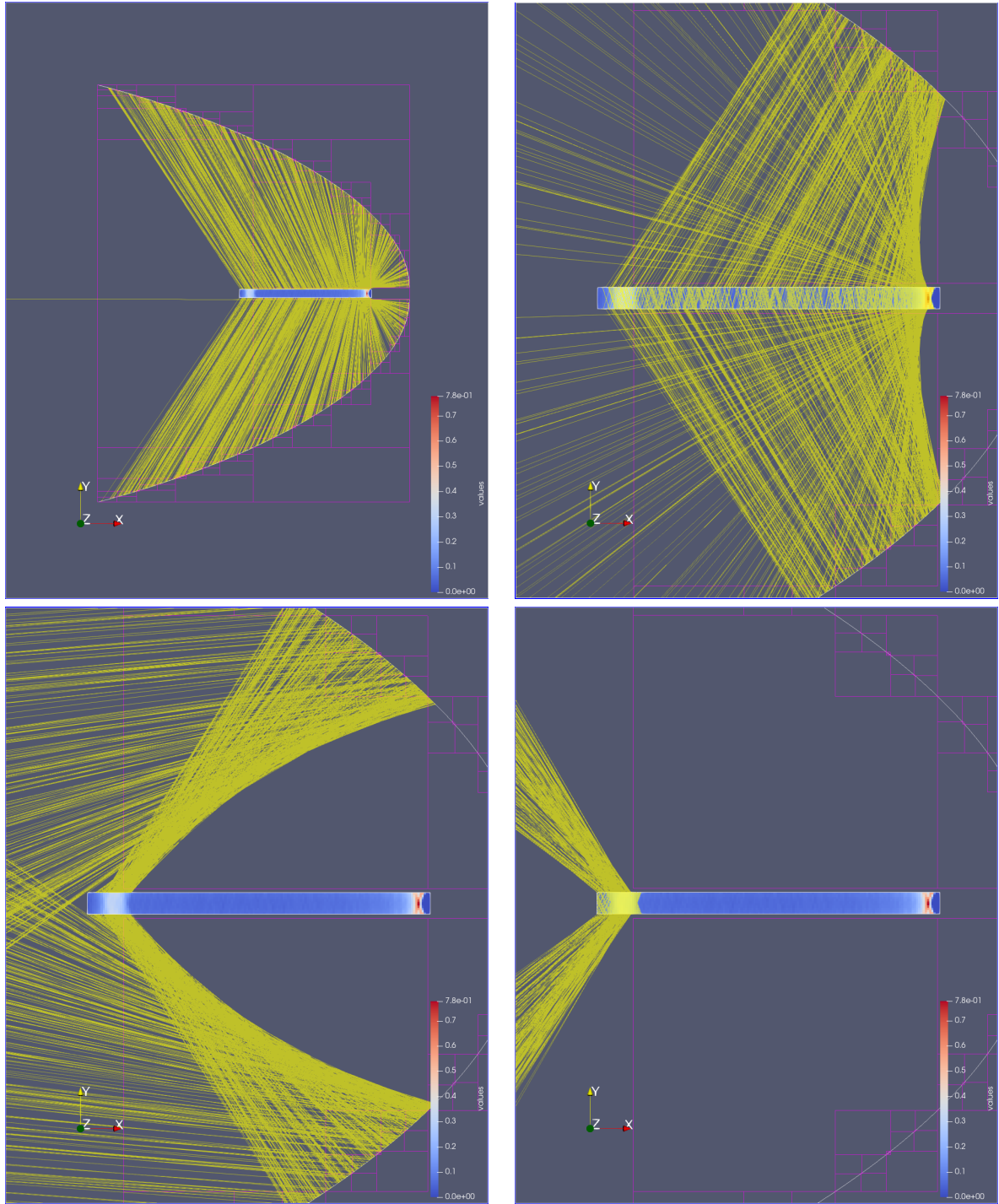


Figure 19: VTK Output for Setup 1 with initial random search for different raytracing depths.

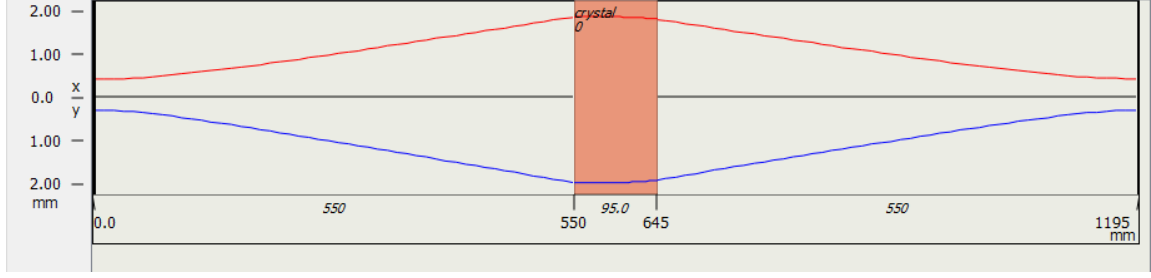


Figure 20: ASLD beam profile for Setup 1 with initial random search.

5.3 Setup 2: Open Crystal Position and open Mirror Endpoints

In Setup 2 the start and end points for the Bezier curve were opened to the optimization algorithm. Additionally, the distance of the laser rod to the focal point of the lens can be altered making the problem a 9 dimensional problem instead of a 4 dimensional one like in Setup 1. Again, the value ranges can be seen in Table 3. The main goal was to improve upon the poor behavior of Setup 1 when it comes to multiple reflections in the pumping process. The first run was done using random search and the second run was started with the mirror in a straight pipe configuration. In the first run the best solution achieved an output power of 38.22 W at a pump power of 690 W, which corresponds to an optical-to-optical efficiency of 5.54%. The lower pump power had to be chosen, as the resonator would become unstable at pump powers above that. The beam quality also significantly improved overall, but the y direction improved more than the x direction. The M^2 quality is 4.03 for the x direction and 1.96 for the y direction. In Figure 5.3 it can be seen that the start configuration after random search is a more conical shape with the crystal closer to the focal point of the lens. BiMADS then adjusted the middle control points so the angle of the mirror becomes shallower and slightly curved inwards. The mirror can be cut at the point where no more rays hit the mirror as it would not be necessary to build such a large mirror and only the shape is important. The shape allows the rays to bounce multiple times from the mirror and thus the crystal is exposed to a higher amount of power on its surface. This can be seen in Table 5.3 for solution 1 as the irradiation efficiency jumped from 130.78% from Setup 1 to 165.70% for Setup 2. It can be also observed that the absorption efficiency actually went down from 16.51% to 15.65% compared to Setup 1. This is likely due to the more perpendicular angle the secondary rays hit the laser rod. This angle diminishes the length of the path of a ray through the laser rod and thus reduces the absorption of the ray in the crystal. This can be seen in Figure 5.3. The beam profile can be seen in Figure 5.3.

As it was noticed that a more shallow conical mirror produces much better results, the same optimization was carried out with a mirror shape resembling a straight pipe as a start point. The start configuration can be seen in Figure 5.3. The resulting mirror shape is similar to the one resulting from the run with initial random search, although towards the laser rod the mirror is more bent and the angle of the mirror is not quite as shallow. It can be seen in Figure 5.3 that solution 1 reflects the secondary rays in a more shallow angle, thus prolonging the lightpath through the gain medium. This effect also reflects in the irradiation efficiency, which can be seen in Table 5.3. It improved from the solution with random search from 165.71% to 171.11% with a similar absorption efficiency. Thus the output beam has a continuous wave output of 38.05 W at a pump power of 665 W, achieving an optical-to-optical efficiency of 5.72%. Again, the pump power had to be limited as otherwise the resonator became unstable. Also, the beam quality improved in both x and y direction. The resulting beam can be seen in Figure 5.3.

| | | |
|-------------------------|---|---------------------|
| Raytracing Settings | Optimization rays | 10000 |
| | Optimization segments | 100 |
| | Final step rays | 100000 |
| | Final step segments | 10000 |
| Optimization Settings | Maximum initial random search black-box evaluations | 10000 |
| | BiMADS Maximum black-box evaluations per MADS run | 1000 |
| | BiMADS constraint type | Progressive barrier |
| | BiMADS poll direction type | Orthogonal N+1 |
| Optimization Parameters | $\mathbf{p}_1.x$ | $[4.2mm, 1000mm]$ |
| | $\mathbf{p}_2.x$ | $[4.2mm, 1000mm]$ |
| | $\mathbf{p}_3.x$ | $[4.2mm, 1000mm]$ |
| | $\mathbf{p}_4.x$ | $[4.2mm, 1000mm]$ |
| | $\mathbf{p}_1.y$ | $[-2000mm, 2000mm]$ |
| | $\mathbf{p}_2.y$ | $[-2000mm, 2000mm]$ |
| | $\mathbf{p}_3.y$ | $[-2000mm, 2000mm]$ |
| | $\mathbf{p}_4.y$ | $[-2000mm, 2000mm]$ |
| | d | $[-300mm, 2000mm]$ |

Table 3: Parameters for Setup 2

| Solution | 1 | 2 | 3 | 4 | 5 | 6 | 7 | 8 |
|----------------------------|---------|---------|---------|---------|---------|---------|---------|---------|
| Absorbed Power[W] | 186.76 | 186.72 | 185.70 | 176.55 | 174.83 | 160.41 | 159.86 | 159.84 |
| Variance[W] | 2.50 | 2.26 | 1.58 | 0.44 | 0.41 | 0.14 | 0.13 | 0.13 |
| Irradiation Efficiency [%] | 165.71 | 165.65 | 165.47 | 156.73 | 155.21 | 136.47 | 136.17 | 136.16 |
| Optical Efficiency [%] | 25.94 | 25.93 | 25.79 | 24.52 | 24.28 | 22.28 | 22.20 | 22.20 |
| Absorption Efficiency [%] | 15.65 | 15.66 | 15.59 | 15.65 | 15.64 | 16.33 | 16.31 | 16.30 |
| cw Output@690W [W] | 38.22 | 37.36 | 36.84 | 30.17 | 32.92 | 22.09 | 21.23 | 21.18 |
| Beam quality x | 4.03 | 4.42 | 4.10 | 4.55 | 4.62 | 4.88 | 4.73 | 4.70 |
| Beam quality y | 1.96 | 3.04 | 2.19 | 4.19 | 4.11 | 4.55 | 4.42 | 4.41 |
| $\mathbf{p}_{1.x}$ [mm] | 4.20 | 4.20 | 4.28 | 4.20 | 4.99 | 4.21 | 4.25 | 4.25 |
| $\mathbf{p}_{2.x}$ [mm] | 251.03 | 246.11 | 248.62 | 357.77 | 354.40 | 403.45 | 402.39 | 402.28 |
| $\mathbf{p}_{3.x}$ [mm] | 510.36 | 524.77 | 541.62 | 696.14 | 697.82 | 691.06 | 691.83 | 691.91 |
| $\mathbf{p}_{4.x}$ [mm] | 778.93 | 777.58 | 774.73 | 992.93 | 992.89 | 999.92 | 999.95 | 999.96 |
| $\mathbf{p}_{1.y}$ [mm] | 30.67 | 29.92 | 27.51 | 24.94 | 23.79 | 10.39 | 10.70 | 10.71 |
| $\mathbf{p}_{2.y}$ [mm] | 853.28 | 856.20 | 855.01 | 834.22 | 832.39 | 791.00 | 793.45 | 793.48 |
| $\mathbf{p}_{3.y}$ [mm] | 1201.00 | 1200.65 | 1121.87 | 1219.69 | 1193.09 | 1378.38 | 1377.93 | 1376.92 |
| $\mathbf{p}_{4.y}$ [mm] | 1465.55 | 1460.93 | 1473.81 | 1591.99 | 1593.16 | 1999.91 | 1999.96 | 1999.96 |
| d [mm] | -299.99 | -299.92 | -294.75 | -267.23 | -267.24 | -236.61 | -236.14 | -236.14 |

Table 4: Pareto optimal points for Setup 2 with initial random search

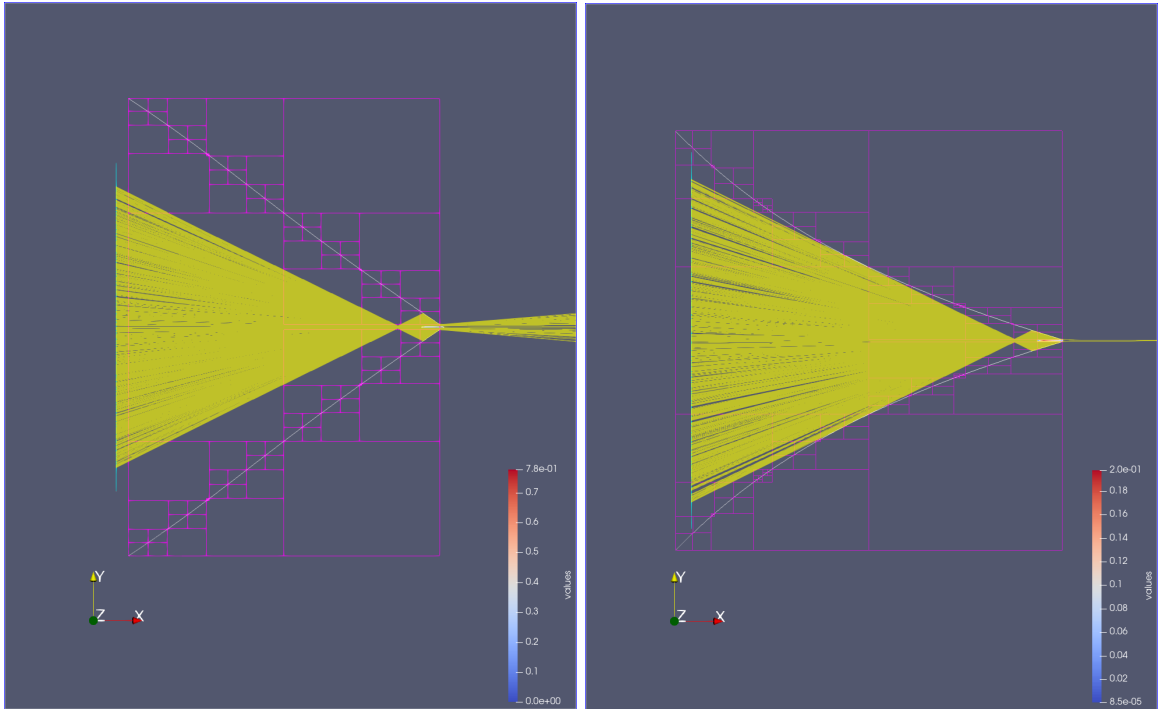


Figure 21: VTK Output for Setup 2 with initial random search

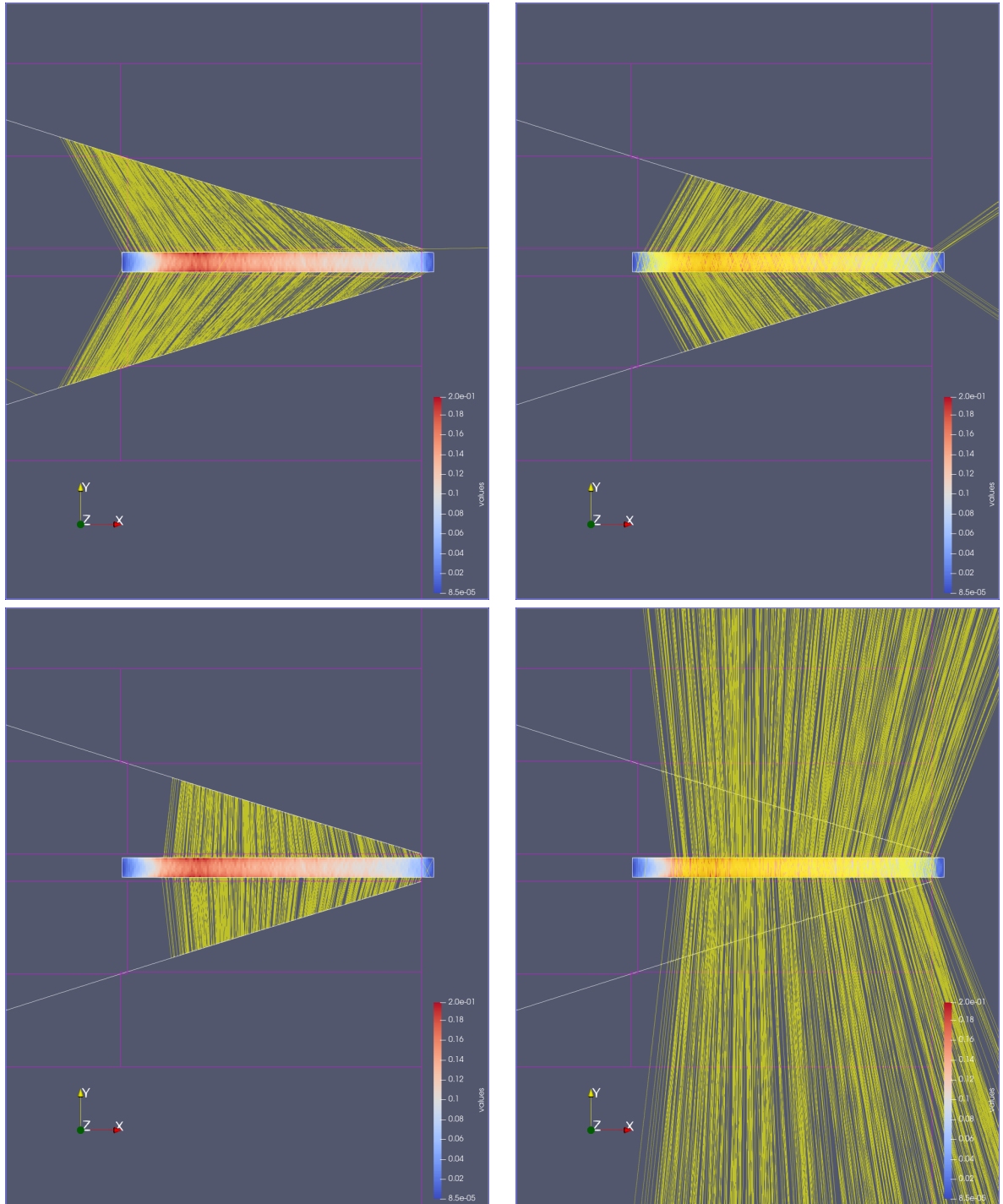


Figure 22: VTK Output for Setup 2 with initial random search for different raytracing depths.

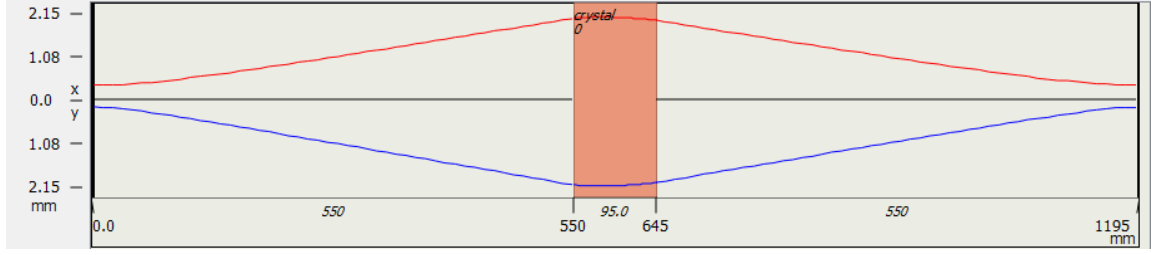


Figure 23: ASLD beam profile for Setup 2 with initial random search.

| Solution | 1 | 2 | 3 | 4 | 5 | 6 | 7 | 8 |
|----------------------------|---------|---------|---------|---------|---------|---------|---------|---------|
| Absorbed Power[W] | 191.13 | 185.11 | 185.70 | 184.50 | 184.50 | 183.38 | 176.90 | 176.84 |
| Variance[W] | 4.08 | 0.66 | 0.58 | 0.58 | 0.58 | 0.51 | 0.31 | 0.31 |
| Irradiation Efficiency [%] | 171.11 | 166.77 | 166.57 | 156.56 | 166.56 | 165.33 | 157.29 | 157.19 |
| Optical Efficiency [%] | 26.55 | 25.71 | 25.63 | 25.62 | 25.62 | 25.47 | 24.57 | 24.56 |
| Absorption Efficiency [%] | 15.51 | 15.42 | 15.39 | 15.38 | 15.38 | 15.40 | 15.62 | 15.63 |
| cw Output@665W [W] | 38.05 | 35.56 | 34.29 | 34.41 | 34.30 | 34.33 | 27.90 | 28.00 |
| Beam quality x | 3.90 | 4.49 | 4.65 | 4.63 | 4.64 | 4.48 | 4.50 | 4.52 |
| Beam quality y | 1.66 | 3.48 | 3.93 | 3.92 | 3.96 | 3.80 | 4.24 | 4.23 |
| $\mathbf{p}_{1..x}$ [mm] | 4.47 | 4.25 | 4.20 | 4.20 | 4.20 | 4.23 | 6.09 | 6.07 |
| $\mathbf{p}_{2..x}$ [mm] | 71.72 | 36.33 | 35.53 | 35.54 | 35.54 | 34.89 | 107.21 | 107.22 |
| $\mathbf{p}_{3..x}$ [mm] | 81.08 | 127.82 | 132.37 | 132.34 | 132.34 | 134.11 | 247.54 | 247.63 |
| $\mathbf{p}_{4..x}$ [mm] | 997.33 | 999.29 | 998.18 | 999.96 | 999.97 | 998.95 | 816.32 | 816.37 |
| $\mathbf{p}_{1..y}$ [mm] | 29.70 | 27.45 | 26.75 | 26.75 | 26.75 | 26.97 | 25.61 | 25.53 |
| $\mathbf{p}_{2..y}$ [mm] | 95.38 | 79.88 | 79.72 | 79.74 | 79.74 | 79.85 | 180.67 | 180.63 |
| $\mathbf{p}_{3..y}$ [mm] | 619.62 | 589.29 | 592.91 | 592.91 | 592.91 | 586.53 | 707.57 | 707.55 |
| $\mathbf{p}_{4..y}$ [mm] | 1209.47 | 1218.32 | 1214.44 | 1213.71 | 1213.69 | 1217.89 | 1886.48 | 1886.5 |
| d [mm] | -264.70 | -281.16 | -280.85 | -280.86 | -280.86 | -278.96 | -242.19 | -242.16 |

Table 5: Pareto optimal points for Setup 2 with initial pipe configuration

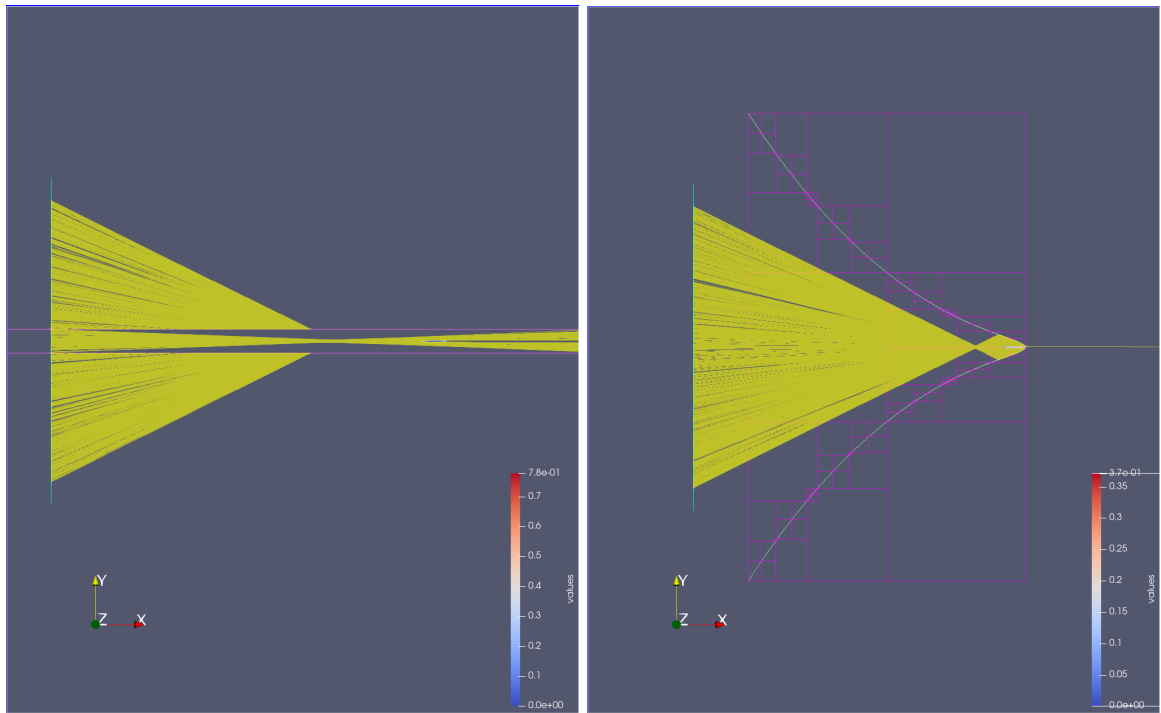


Figure 24: VTK Output for Setup 2 with pipe start configuration

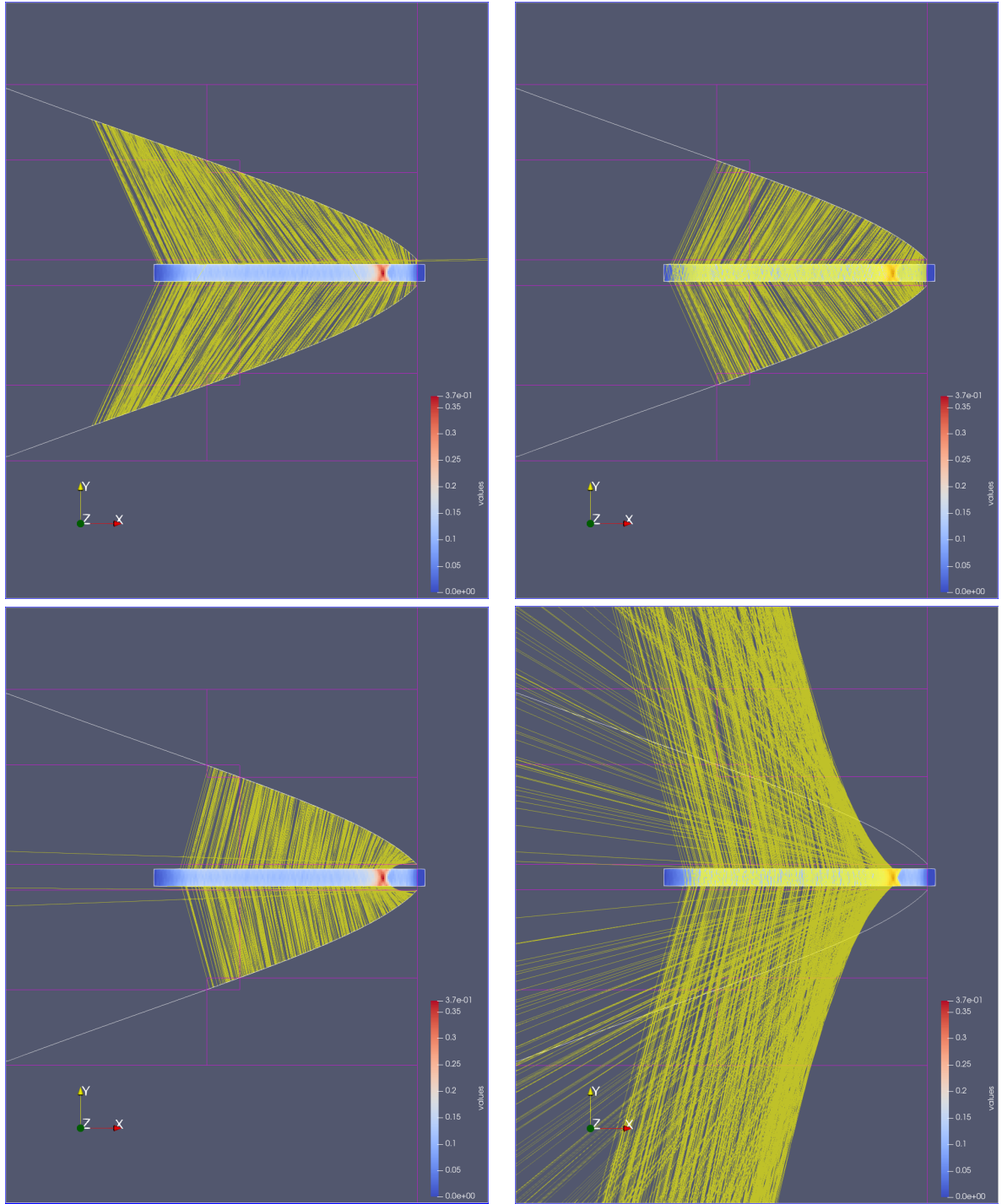


Figure 25: VTK Output for Setup 2 with pipe start configuration for different raytracing depths.

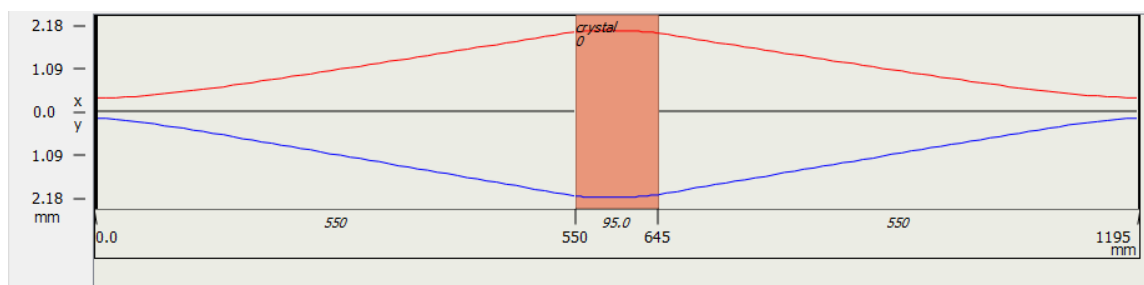


Figure 26: ASLD beam profile for Setup 2 with pipe start configuration.

6 Conclusion

Ray tracing techniques are well suited to optimize pump light absorption in a gain medium. It was shown that for a solar laser, where many optical effects such as divergence of sunlight or dispersion effects in different media, the power absorption and variance across the crystal can be optimized using a biobjective mesh adaptive direct search algorithm (BiMADS). The resulting beam output of the Pareto front was then analysed using ASLD. Here, a solution was found that achieves a continuous wave power output of 38.05 W at a pump power of 665 W, which corresponds to a optical-to-optical efficiency of 5.72%. Compared to an algebraically derived reference solution this is an improvement of 34.9% in terms of output power. Additionally, the beam quality was improved significantly. It was found that mainly the angle of incidence of rays on the crystal and the absorption of secondary rays contribute the most to the final output power of the beam. The optimization of objective functions resulting from a raytracing simulation proved to be nonsmooth and sometimes even discontinuous. For this reason derivative free algorithms should be chosen to optimize the input parameters. It was found that the MADS algorithm performed quite well finding local minima and using the BiMADS algorithm to apply MADS even biobjective functions can be optimized. The inner workings and the theory behind them was examined in detail. The resulting pareto front of solutions can then be filtered for solutions that offer the best compromise between the two objective functions for the task at hand. The black-box functions evaluated in this type of optimization can be computationally expensive, but the more the function is evaluated the more accurate the results are. For this reason the raytracing simulation should be as optimized as possible while still offering physically accurate results. Thus a 2D raytracing framework was developed which applies raytracing techniques commonly used in image processing. The framework was then used as a black-box function for the BiMADS algorithm to optimize geometrical parameters in a setup of a Nd:YAG solar laser. It models optical effects such as Snell's law, the Fresnel laws and Sellmeier dispersion accurately. Unfortunately the beam analysis software does not model the Fresnel laws, thus the framework had to be adjusted to do the same to deliver comparable results. In the future one could even integrate an optimizer directly into a beam analysis software and optimize on beam quality and continuous wave output objective functions directly. Nevertheless the principle of derivative free optimization can still be applied and thus the geometrical setup can be optimized.

References

- [1] John Amanatides, Andrew Woo, et al. A fast voxel traversal algorithm for ray tracing. In *Eurographics*, volume 87, pages 3–10, 1987.
- [2] C. Audet and J.E. Dennis, Jr. Mesh adaptive direct search algorithms for constrained optimization. *SIAM Journal on Optimization*, 17(1):188–217, 2006.
- [3] C. Audet, S. Le Digabel, V. Rochon Montplaisir, and C. Tribes. The NOMAD project. Software available at <https://www.gerad.ca/nomad/>.
- [4] Charles Audet, Gilles Savard, and Walid Zghal. Multiobjective optimization through a series of single-objective formulations. *SIAM Journal on Optimization*, 19(1):188–210, 2008.
- [5] GJCL Bruls. Exact formulas for a thin-lens system with an arbitrary number of lenses. *Optik*, 126(6):659–662, 2015.
- [6] Frank H Clarke. Nonsmooth analysis and optimization. In *Proceedings of the international congress of mathematicians*, volume 5, pages 847–853. Citeseer, 1983.
- [7] Laura Corner. Introduction to laser physics. https://www.google.com/url?sa=t&rct=j&q=&esrc=s&source=web&cd=&cad=rja&uact=8&ved=2ahUKEwjuxZK2tvP2AhX08LsIHU-kCugQFnoECAYQAQ&url=https%3A%2F%2Findico.cern.ch%2Fevent%2F759579%2Fcontributions%2F3184719%2Fattachments%2F1810600%2F3003248%2F%2FL_Corner_Introduction_to_Laser_Physics.pdf&usg=AOvVawOn0-uNGRjVKHzUSAAaXGk1, 2019. [Online; accessed 1-April-2022].
- [8] Jeffrey Larson, Matt Menickelly, and Stefan M Wild. Derivative-free optimization methods. *Acta Numerica*, 28:287–404, 2019.
- [9] S. Le Digabel. Algorithm 909: NOMAD: Nonlinear optimization with the MADS algorithm. *ACM Transactions on Mathematical Software*, 37(4):1–15, 2011.
- [10] Dawei Liang and Joana Almeida. Highly efficient solar-pumped nd: Yag laser. *Optics express*, 19(27):26399–26405, 2011.
- [11] OpenGL. Opengl mathematics (glm). <https://glm.g-truc.net/0.9.4/api/index.html>. [Online; accessed 28-March-2022].
- [12] RP Photonics. Abcd matrix. https://www.rp-photonics.com/abcd_matrix.html. [Online; accessed 7-April-2022].
- [13] RP Photonics. Four-level and three-level laser gain media. https://glm.g-truc.net/0.9.4/api/index.htmlhttps://www.rp-photonics.com/four_level_and_three_level_laser_gain_media.html. [Online; accessed 1-April-2022].
- [14] RP Photonics. M2 factor. https://www.rp-photonics.com/m2_factor.html. [Online; accessed 26-April-2022].
- [15] Will Schroeder, Ken Martin, and Bill Lorensen. *The Visualization Toolkit (4th ed.)*. Kitware, 2006.
- [16] A. E Siegman. *Lasers*. Mill Valley, Calif.: University Science Books, 1986.
- [17] Multiphysics Laser Simulation Software. Asld. <http://www.asldweb.com/index.html>.
- [18] Justin Solomon. *Numerical algorithms: methods for computer vision, machine learning, and graphics*. CRC press, 2015.
- [19] Marc Stamminger. Global Illumination SS21, 2021.
- [20] Wikipedia. Solar-pumped laser. https://en.wikipedia.org/wiki/Solar-pumped_laser. [Online; accessed 2-April-2022].
- [21] Takashi Yabe, Kunio Yoshida, and Shigeaki Uchida. Demonstrated fossil-fuel-free energy cycle using magnesium and laser. In *International Congress on Applications of Lasers & Electro-Optics*, volume 2007, page M1103. Laser Institute of America, 2007.

- [22] David E Zelmon, David L Small, and Ralph Page. Refractive-index measurements of undoped yttrium aluminum garnet from 0.4 to 5.0 μm . *Applied optics*, 37(21):4933–4935, 1998.